International Journal of Pharmaceutics 640 (2023) 123019

Contents lists available at ScienceDirect

International Journal of Pharmaceutics

journal homepage: www.elsevier.com/locate/ijpharm

Liquid crystalline nanoparticles enable a multifunctional approach for topical psoriasis therapy by co-delivering triptolide and siRNAs

Ana Vitória Pupo Silvestrini [a], Fabíola Garcia Praça [a], Marcel Nani Leite [b,c], Márcia Carvalho de Abreu Fantini [c], Marco Andrey Cipriani Frade [b,c], Maria Vitória Lopes Badra Bentley [a,*]

[a] School of Pharmaceutical Sciences of Ribeirao Preto, University of Sao Paulo, 14040-903, Ribeirao Preto, SP, Brazil
[b] Division of Dermatology, Department of Internal Medicine, Ribeirão Preto Medical School, University of São Paulo, Ribeirão Preto, SP, Brazil
[c] Institute of Physics, University of Sao Paulo, 05508-900, São Paulo, SP, Brazil

ARTICLE INFO

Keywords:
Skin delivery
Liquid crystalline nanoparticle
Psoriasis
Small interfering RNA
Triptolide

ABSTRACT

Liquid crystalline nanoparticles (LCNs) are an attractive drugs topical delivery system due to the great internal ordering, wide interfacial area and structural similarities with the skin. In this work, LCNs were designed to encapsulate triptolide (TP) and to complex on its surface small interfering RNAs (siRNA) targeting TNF-α and IL-6, aiming at topical co-delivery and regulating multi-targets in psoriasis. These multifunctional LCNs showed appropriate physicochemical properties for topical application, such as a mean size of 150 nm, low polydispersion, TP encapsulation greater than 90% and efficient complexation with siRNA. The internal reverse hexagonal mesostructure of LCNs was confirmed by SAXS while their morphology was assessed by cryo-TEM. *In vitro* permeation studies revealed an increase of more than 20-fold in the distribution of TP through the porcine epidermis/dermis was achieved after the application of LCN-TP or LCN TP in hydrogel. In cell culture, LCNs showed good compatibility and rapid internalization, which was attributed to macropinocytosis and caveolin-mediated endocytosis. Anti-inflammatory potential of multifunctional LCNs was assessed by reducing of TNF-α, IL-6, IL-1β and TGF-β1 levels in LPS-stimulated macrophages. These results support the hypothesis that the co-delivery of TP and siRNAs by LCNs may be a new strategy for psoriasis topical therapy.

1. Introduction

Current advances and exponential growth in nanotechnology research have opened new frontiers for the design of multifunctional nanoparticles that go beyond simple, inert platforms (Karimi et al., 2016; Shan et al., 2022). In this context, lyotropic liquid crystalline nanoparticles (LCNs), an emerging class of nanomaterials, are considered promising drug delivery systems, due to their highly ordered organization in two- and three-dimensional structures that are suitable to accommodate and release in a controlled manner peptides, proteins, nucleic acids, hydrophilic and hydrophobic small molecules and imaging agents (Silvestrini et al., 2022; van 't Hag et al., 2017). Furthermore, it is possible to adapt their surfaces to adjust their characteristics to specific medical applications, for example, coating with load-bearing polymers, stimulus-responsive ones, or else bioligands for targeting cells/tissues (Silvestrini et al., 2022). In particular, due to structural similarity to the skin microstructure, an improvement in penetration and therapeutic effects has been reported of different actives delivered on these platforms, such as chemotherapeutic agents, photosensitizers, hormones, anti-inflammatories, anti-aging agents, nucleic acid and vaccines (Silvestrini et al., 2020; Tan et al., 2019).

Research into new treatments for skin diseases, particularly psoriasis, has led to selective therapeutics directed to specific molecular targets (Armstrong and Read, 2020; Hawkes et al., 2017). Therefore, therapy with antisense oligonucleotides targeting key inflammatory mediators such as tumor necrosis factor alpha (TNF-α), interleukin (IL)-6, IL-36 and others has shown promising results and progress in disease control (Boakye et al., 2017; Depieri et al., 2016; Lee et al., 2022, 2020; Mandal et al., 2020; Nemati et al., 2017; Rosa et al., 2018). In this work, we chose antisense therapy by RNA interference using small interfering RNA (siRNA) because it has gained importance in academic research and the pharmaceutical industry due to its highly specific effects, especially

* Corresponding author at: Av. do Cafe, s/n, 14040-903 Ribeirao Preto, SP, Brazil.
E-mail address: vbentley@usp.br (M.V.L. Badra Bentley).

https://doi.org/10.1016/j.ijpharm.2023.123019
Received 10 January 2023; Received in revised form 27 April 2023; Accepted 1 May 2023
Available online 4 May 2023

after the approval of the first siRNA drug, Patisiran, in 2018 by United States Food Drug Administration (Caillaud et al., 2020; Yan et al., 2022). The siRNA acts in the post-transcriptional phase by specifically binding the messenger RNA (mRNA) of the target gene and preventing or reducing the translation of the mRNA into the encoded protein (Setten et al., 2019).

Due to the physicochemical disadvantages of siRNA molecules, various strategies are employed to promote effective delivery, with carriers offering protection and stability of the delivered molecule being the most desirable (Caillaud et al., 2020; Setten et al., 2019). Non-viral vectors such as nanoparticles have proven to be effective in intracellular delivery and gene silencing (Yan et al., 2022). For example, our group has reported successful siRNA delivery and associated gene silencing with reverse hexagonal LCNs and other lipid nanoparticles against skin diseases (Campos et al., 2020; Depieri et al., 2016; Petrilli et al., 2016; Suzuki et al., 2021; Tofani et al., 2018; Viegas et al., 2020). To date, it is known that modifying the surface of nanoparticles with cationic agents promotes efficient loading of siRNA molecules (Kim et al., 2019). Recently, it was found that the surface of nanoparticles modified with poly(allylamine hydrochloride) (PAH), a polycation containing primary amines, exhibited high rates of intracellular delivery of siRNA as well as the release of its contents as a function of pH (Han et al., 2015; Suzuki et al., 2021). At an endolysosomal pH, protonation of the PAH amine groups leads to osmotic swelling, which facilitates translocation of siRNA and ultimately gene silencing (Andreozzi et al., 2017; Di Silvio et al., 2019).

In addition, we chose a natural compound called triptolide (TP), a phytoactive present in the Chinese herb *Tripterygium wilfordii* Hook. F. (TWHF), which has a remarkable range of therapeutic effects evidenced by its immunosuppressive, anti-inflammatory, and antitumor properties *in vitro* and *in vivo* (Tong et al., 2021; Yuan et al., 2019). Clinical trials have demonstrated the antipsoriatic potential of TP alone and in crude TWHF plant preparations. However, its low water solubility and oral bioavailability as well as adverse effects have limited its clinical application (Ren et al., 2021; Tong et al., 2021). To overcome these disadvantages of TP and enable co-administration with siRNAs, we propose a nanostructured delivery system based on liquid crystal. Thus, siRNAs targeting the TNF-α and IL-6 were combined with TP in cationic reverse hexagonal LCNs to achieve a synergistic anti-inflammatory effect (see Fig. 1). LCNs exhibited greater co-delivery of topical drugs, which was higher when LCNs were embedded in hydroxyethylcellulose hydrogel. The LCN hydrogel exhibited rheological and bioadhesive behavior suitable for topical application. Finally, therapeutic efficacy was evaluated in an inflammation model using lipopolysaccharide (LPS)-stimulated primary human monocytes *in vitro*. The characterization of this new platform and its mechanisms of cellular internalization and endosomal escape are discussed in detail in this article. In short, for the first time, the co-administration of two different siRNAs and TP in a single delivery system has been validated, opening new possibilities for topical therapy of psoriasis and other inflammatory skin diseases.

2. Materials and methods

2.1. Chemical and reagents

Monoolein (MO) was used in the form of Myverol® 18–99 k and was

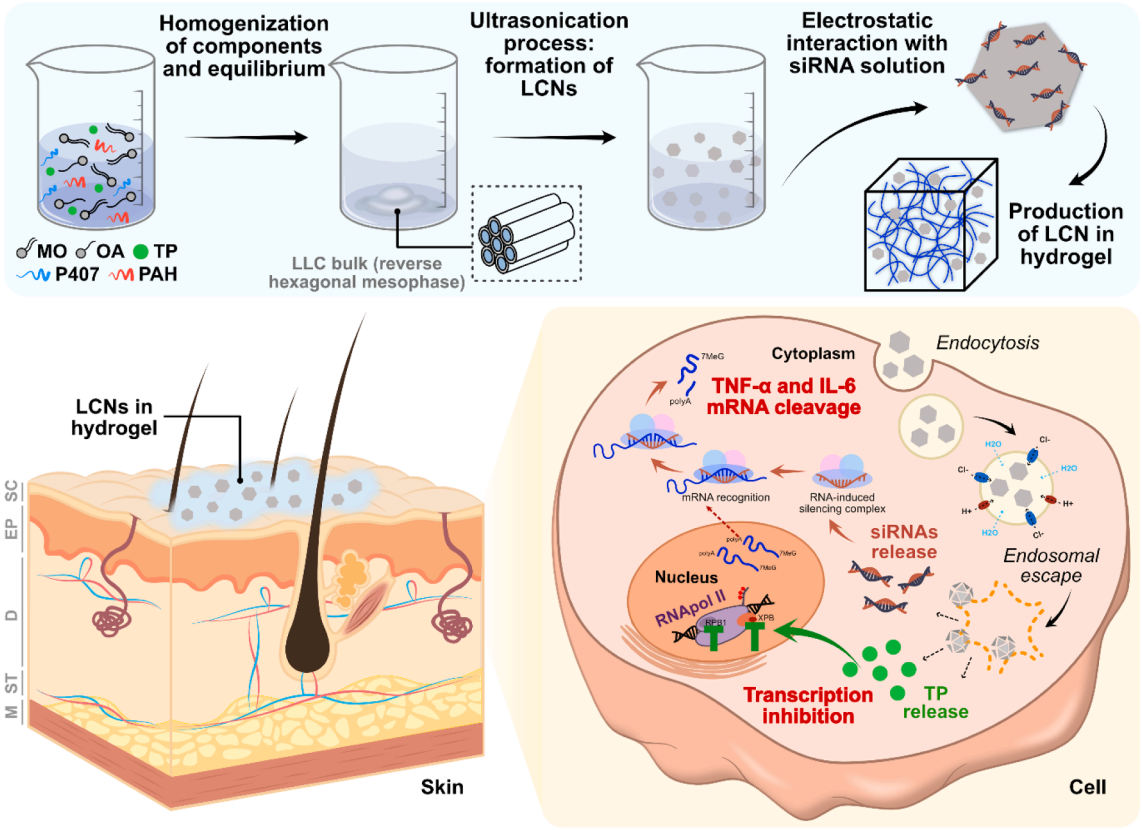

Fig. 1. Graphic summary of LCN production and functional *in vitro* studies. Top-down approach to production of reverse hexagonal LCN dispersions based on monolein, oleic acid, PAH and P407 co-loaded with TP and dual siRNAs, and formation of hydrogel containing the dispersions. Representative penetration and retention of LCNs in skin membrane, mainly in the epidermal region. Cell internalization via caveolin-mediated macropinocytosis and endocytosis, and efficient endosomal escape with subsequent knowdown by siTNF-α and siIL-6; and blocking of RNA polymerase II (RNApol II) subunits by TP binding and downregulation of mediators and pro-inflammatory pathways. Abbreviations: LLC – lyotropic liquid crystal; SC – stratum corneum; EP – epidermis; D – dermis; ST – subcutaneous tissue; M – muscle; and mRNA – messenger RNA.

kindly donated by Kerry Group (Ireland). Oleic acid (OA), poloxamer 407 (P407), PAH (molecular weight 15 kDa; and 10.69 mmol of amine groups), TP (>98% purity), DAPI (4′, 6-diamidine-2′-phenylindole dihydrochloride) dye, rhodamine 123 dye, DND-26 green dye plain tracer, Dulbecco Modified Eagle Medium (DMEM), Roswell Park Memorial Institute (RPMI)-1640 culture medium, fetal bovine serum (FBS), antibiotic and antimycotic solution stock (amphotericin B, streptomycin and penicillin), trypsin-EDTA, resazurin, propidium iodide, Histopaque 1077, lipopolysaccharide (LPS) from *Salmonella enterica* serotype *typhimurium* and endocytic pathway inhibitors (philipin III from *Streptomyces filipinensis*; cytochalasin D from *Zygosporium mansonii*; cytochalasin B from *Drechslera dematioidea*, sucrose, methyl-β-cyclodextrin, chlorpromazine hydrochloride, amiloride hydrochloride, and sodium azide) were obtained from Sigma-Aldrich (USA). Hydroxyethylcellulose polymer (HEC; Natrosol® 250 HHr) was obtained from Aqualon™ (USA). Lipofectamine 2000® and Quant-iT™ RiboGreen® RNA Reagent kit were acquired from Invitrogen (Carlsbad, CA, USA). Sodium heparin (5000 IU/mL) was obtained from Blausiegel (Brazil). The GelRed® dye (nucleic acid gel stain) was obtained from Biotium, Inc. (USA). RNAse-free water with diethylpyrocarbonate (DEPC), *Silencer*® negative control siRNA (#AM4635), *Silencer*® pre-engineered TNF-α siRNA (Cat #AM16706, ID 188363, sense sequence CGUCGUAGCAAACCACCAATT and antisense sequence UUGGUGGUUUGCUACGACGTG) and IL-6 siRNA (Cat #AM16704, ID 144576, sense sequence GGACAUGACAACUCAUCUCTT and antisense sequence GAGAUGAGUUGUCAUGUCCTG) were obtained from Ambion™ (USA). AlexaFluor 647 (AF647)-labeled AllStars Negative Control siRNA (#1027295) was obtained from Qiagen® (Germany). Reagents and antibodies for immunoassays were purchased from BD Biosciences (USA). All other chemical reagents were of analytical purity and commercially available.

2.2. UV–Vis HPLC method for TP quantification

The Shimadzu (Kyoto, Japan) high-performance liquid chromatography (HPLC) system with a LiChrospher® 250 RP-18 reversed-phase chromatography column (250 × 4.6 mm long, 5 μm, LiChrospher; Merck, Germany) was used to quantify TP in the studies. The isocratic mobile phase was an acetonitrile–water mixture (70:30, v/v) acidified with 0.02% (v/v) orthophosphoric acid (pH 4.5), and the flow rate was set at 0.9 mL/min. The temperature of the column was set at 25 °C, the detection wavelength was kept at 218 nm (UV–visible) and an injection volume of 40 μL was used. The method was linear in the concentration range from 0.1 to 12.5 μg/mL, and the calibration curve was $y = 167898x - 620.56$ ($r = 0.999$). The error and accuracy of the method had a coefficient of variation that did not exceed 0.5% and 99%, respectively. The lower limit of quantification and detection of the method were 0.05 μg/mL and 0.025 μg/mL, respectively. The recovery rate of TP on the skin was 95% and 99% for the lowest and highest concentrations, respectively.

2.3. LCN and LCN-hydrogel preparation

LCNs consisting of MO, OA, PAH polymer, and the aqueous phase (0.01 M sodium phosphate buffer, pH 7.0, with 1% P407 in DEPC water) were prepared at a ratio of 8:1:0.5:89.5 (w/w/w/w) according to the method described previously (Lopes et al., 2006; Rossetti et al., 2011). Briefly, the bulk of the reverse hexagonal mesophase was obtained by mixing the melted MO (42 °C) with the OA in the presence or absence of TP (0.04%, w/w), and then the aqueous phase containing the polymer was added. After 24 h of equilibration, the system was sonicated in an ice bath at 30% maximum power for 1 min (Bandelin Electronic Sonicator, UW2200, Germany). For the assays, siRNA was incubated with the LCN for 30 min at room temperature.

To increase the viscosity of the LCNs, the thickening polymer HEC (1.0%, w/v) was added to the final dispersion by sonication and magnetically stirred at 300 rpm for 6 h at room temperature.

2.4. Physical-chemical characterization

2.4.1. Polarized light microscopy

The bulk liquid-crystalline mesophases were analyzed using an optical microscope with circular polarized light (Axioplan 2 Image Pol microscope, Carl Zeiss, Oberkochen, Germany) equipped with an LD-AchroPlan 32x/0.40 objective set, fitted with a video camera Axiocan HRc (Carl Zeiss AG, Germany). The systems were observed at room temperature.

2.4.2. Size, polydispersity index, zeta potential and density of LCN

The intensity-weighted average hydrodynamic diameter (Z-average) and polydispersity index (PdI) were analyzed by dynamic light scattering (DLS) using a Malvern Zetasizer Nano (Malvern Instruments, Worcestershire, UK). Measurements of particle electrophoretic mobility were expressed as a zeta potential using the provided software (Malvern, UK). All measurements were performed in triplicate at 25 °C. Data were means of three determinations in different batches of the same dispersion type.

NTA experiments were performed with a NanoSight NS300 (Malvern Instruments, Worcestershire, UK) equipped with a camera and a 642-nm laser (output power 40 mW) and used to determine nanoparticle concentration (number of particles per mL). The formulations were diluted in ultrapure water (1:5000, v/v) and the measurements were performed at 25 °C. Results were reported as particle concentration (mean ± standard error) determined using the NTA software.

2.4.3. TP entrapment efficiency (EE)

The content of entrapped TP was determined by an indirect method involving ultracentrifugation through an Amicon® Ultra centrifugal filter (50 kDa; Millipore, Darmstadt, Germany) according to the manufacturer's recommendations. The TP in the ultrafiltrate was quantified by the HPLC method and the EE was calculated according to the formula: EE (%) = [(theoretical concentration – calculated concentration)/theoretical concentration)] × 100.

2.4.4. siRNA binding and integrity of complex LCN-siRNA

The efficiency of LCN and siRNA binding was investigated by gel retardation assay using 2% agarose gel. LCN complexes were formed with 5 μM siRNA control and incubated at room temperature for 30 min. Then, each sample was added to GelRed® (nucleic acid staining solution). To assess the release of siRNA and its integrity, a heparin solution (5000 IU/mL) was added to the LCN-siRNA complex for 60 min at 37 °C, followed by the addition of GelRed®. Electrophoresis was performed at a voltage of 100 V for 20 min in 1 × Tris-acetate-EDTA buffer (pH 8). Visualization and acquisition of images were performed using a UV light system (Transluminator, Loccus Biotechnology, Brazil).

RiboGreen® assay was performed to quantify the complexation efficiency of siRNA (5 μM) in LCNs. Low-range and high-range calibration curves using standard ribosomal RNA and control siRNA were prepared, according to the manufacturer, and used to calculate the complexation efficiency of the LCNs. The LCN-siRNA complex were diluted with TE buffer and analyzed using spectrofluorometer (excitation 500 nm, emission 525 nm). The efficiency of LCN siRNA complexing was calculated by dividing the concentration of free siRNA quantified by the initial concentration of siRNA and multiplying by 100%.

2.4.5. Small angle X-ray scattering (SAXS)

SAXS experiments were performed using a Xeuss® 2.0 (Xenocs) setup with a Pilatus bidimensional detector, operating at a wavelength of 1.5418 Å (copper tube) and sample to detector distance of 0.9 m. At this configuration, the measured q range covers 0.015 $Å^{-1}$ up to 0.43 $Å^{-1}$. Special glass capillaries (2.0 mm diameter) containing samples were placed in a temperature-controlled (23 °C) sample holder. In order to obtain absolute scattering intensities, the background scattering intensities, the background scattering was removed, taking the data of

0.01 M sodium phosphate buffer (pH 7.0). The data treatment (azimuthal integration, background subtraction and absolute scale normalization) was performed using Python programs developed by Complex Fluids Group of Institute of Physics - São Paulo University. The scattering vector, q, was determined from the scattering angle using the relationship $q = (4\pi/\lambda)\sin\theta$, were 2θ being the scattering angle and λ being the wavelength of radiation. To identify the mesophase type, the scattering vector (q) values of the peaks were correlated with Miller indices for known mesophases.

2.4.6. Cryogenic transmission electron microscopy (Cryo-TEM)

Cryo-TEM measurements were performed in a Talos F200C microscope (Thermo, USA), operating at 200 kV, with a Ceta 16 M 4 k × 4 k camera (Thermo, USA) for digital image acquisition. The lacey carbon film on a 300-mesh copper grid (Ted Pella®, USA) were previously treated with a load of 25 mA for 50 s, in an EasiGlow (I) equipment (Ted Pella®, USA) and the vitrification of samples Vitrobot Mark IV (Thermo, USA). The sample was applied to each grid (3 μL), performing the excess draining step (Blot time 3 and Blot force–3) and freezing the grids immediately in liquid ethane. After this step, the grids were kept in liquid nitrogen until insertion under the microscope. ImageJ® software was used to image analysis of Cryo-TEM micrographs.

2.5. Physical and chemical stability studies

The stability of the LCN was determined over a period of 90 days at room temperature (25 °C), low temperature (4 °C), and high temperature (40 °C). Physical stability was monitored by measurements of Z-average size, PdI, and zeta potential. Chemical stability was determined by the amount of encapsulated TP. Data were averages of three determinations in three batches of the same dispersion type.

2.6. Rheological and mechanical aspects of LCN hydrogel

Rheological evaluation was performed using a Discovery HR-2 Hybrid Rheometer (TA Instruments, New Castle, DE) with cone plate configuration connected to the software program TRIOS. Measurements were made at 32 °C with a shear gradient of 0 to 1000 s^{-1} for 150 s, and maximum shear was maintained for 20 s until the sloping curve began. Mean values were calculated from at least three independent experiments, each with three technical replicates.

Texture (hardness, cohesiveness, and adhesiveness) and bioadhesion strength in a hydrogel skin model were determined in TA.XT Plus (Stable Micro Systems Ltd., Surrey, UK), Exponent Software (Stable Micro Systems, UK). Texture measurements were made with an analytical probe (10 mm diameter) connected to the instrument and moved over the sample (10 g hydrogel) at a speed of 1 mm/s, a depth of 15 mm, and a return speed of 2 mm/s. To determine bioadhesion strength, hydrogels were added to an analytical probe (13 mm in diameter) connected to the equipment. The analytical probe was moved at a speed of 0.1 mm/s against the porcine skin fragment attached to an acrylic disk, maintaining a compressive force of 0.5 N for 1 min. The force required to dislodge the hydrogels from the porcine skin was measured. For each formulation, five replicates were performed at room temperature so that the same conditions existed for each measurement.

2.7. In vitro vertical diffusion cell studies

2.7.1. Drug release

The drug release kinetics of LCNs were evaluated using cellulose membrane dialysis (molecular weight cut-off 12000; Himedia Labs, India) in a Franz vertical diffusion cell (Hanson Instruments, USA) with a diffusion area of 1.77 cm^2, performed according to the methodology previously described by Praça et al. (Praça et al., 2018). The formulations (TP solution, TP hydrogel, LCN TP, and LCN TP hydrogel) were applied to the receptor compartment. After 0.5, 1, 2, 4, 6, 8, 10, 12, and 24 h, the receptor solution was collected, and the amount of TP was determined by HPLC (n = 5). This assay was performed under infinite dose, occlusion and sink conditions. The cumulative release (%) as a function of time (t) was plotted and fitted using zero-order, first-order, and Higuchi models.

2.7.2. Cutaneous permeation and retention

In vitro experiments were performed using swine ear skin as a biological membrane (500 μm). The samples and conditions were the same way as for release kinetics. To evaluate skin retention in SC and epidermis (without SC) plus dermis (EP + D), the skins were removed from the Franz vertical diffusion cell at the end of each predetermined time (2, 4, 6, 8, and 12 h) and the surfaces were peeled off with 15 adhesive strips, followed by extraction in acetonitrile. The remaining skin (EP + D) was homogenized in acetonitrile (Marconi, Turrax MA102, Brazil) and treated in an ultrasonic bath (QUIMIS®, Q3350, Brazil) for 1 min and 20 min, respectively. The extracted TP was quantified by HPLC (n = 5).

The intensity and penetration depth of the investigated LCN-siRNA AF647 (5 μM) into the skin were examined using confocal microscopy analysis (Leica TCS SP8 CLSM microscope, Leica Microsystems Inc., Buffalo Grove, IL, USA). The histological cryo-sections were stained with DAPI (0.3 μg/mL) and images were then acquired with an objective immersion of 63 nm and lasers of $\lambda = 405$ nm and $\lambda = 638$ nm suitable for DAPI and AF647, respectively.

2.8. Cellular studies

2.8.1. Human immortalized non-tumorigenic keratinocyte cell line

Human immortalized non-tumorigenic keratinocyte cell line, HaCaT cells, were obtained from the American Type Culture Collection (ATCC). Cells were cultured in DMEM supplemented with 10% heat-inactivated FBS and 1% (v/v) of an antibiotic and antifungal solution at 37 °C in a humidified atmosphere containing 5% CO_2.

2.8.2. Cell viability assay

HaCaT cells were seeded into a 96-well plate (10^4 cells/well) and incubated for 15 h to allow the cells to adhere. Then the culture medium was removed and the samples (free TP, naked siTNF-α/siIL-6, LCN without PAH; LCN TP without PAH; LCN TP; LCN-siTNF-α; LCN-siIL-6; LCN-siTNFα-siIL-6, LCN TP-siTNF-α, LCN TP-siIL-6, and LCN TP-siTNF-α-siIL-6) suspended in fresh culture medium were added to the well at various concentrations. After 24 h of incubation, cell viability was assessed by adding resazurin (25 μg/mL) for 4 h, and measurements were performed according to the manufacturer's instructions (excitation: 530/25, emission: 590/35). Half-maximal inhibitory concentration (IC_{50}) was determined from the dose–response curve by linear regression and estimated from the fitted line.

2.8.3. Cellular uptake

Flow cytometry and fluorescence microscopy were used to study the cellular uptake of LCN-siRNA and intracellular distribution in HaCaT cells. Cells (5×10^5 cells/well) were incubated for 1, 2, 6, 12, and 24 h with samples at a final concentration of 40 nM siRNA AF647 (naked siRNA; Lipofectamine 2000® siRNA and LCN-siRNA). After trypsinization, centrifugation, and pelleting, cells were resuspended in PBS and subjected to flow cytometry (BD FACSCanto™ I Flow Cytometry System, BD Biosciences, US).

To study the fluorescence images, HaCaT cells were seeded in 35-mm glass-bottom plates (10^5 cells/well) and samples were added at the above concentration for 6 h. Cells were fixed with paraformaldehyde (2%; 10 min) and stained with DAPI (0.3 μg/mL; 10 min) for nucleus staining and rhodamine 123 (1.0 μg/mL; 5 min) for mitochondrial membrane. Coverslips were transferred to a glass slide with a drop of Fluoromount™. Finally, fluorescence images of the cells were acquired using a 63 × oil immersion objective under a CLSM (excitation/

emission: 652/670 nm for AF647; 358/461 nm for DAPI; and 507/529 nm for Rhodamine 123).

The detailed mechanism of LCN-siRNA uptake was investigated by various pretreatments with endocytosis inhibitors. HaCaT cells (5×10^5 cells/well) were individually pretreated with concentrations of non-toxic inhibitors: (1) 50 mM sodium azide; (2) Philippine III 50 μM; (3) 30 μM cytochalasin D; (4) 1 μM cytochalasin B; (5) 0.5 M sucrose; (6) 1 μM methyl-β-cyclodextrin (MβC); (7) 2.5 μM chlorpromazine hydrochloride; and (8) 0.1 mM amiloride hydrochloride. After one hour of pretreatment, the inhibitor solutions were removed and LCN siRNA AF647 was added and incubated for 6 h. After trypsinization, centrifugation, and pelleting, cells were resuspended in PBS and subjected to flow cytometry (BD FACSCanto™ I Flow Cytometry System, BD Biosciences, US). Propidium iodide (excitation/emission: 535/617 nm) was used to determine cell viability and cell uptake was calculated using the AF647 signal from the detector (excitation/emission: 652/670 nm).

Intracellular trafficking and *endo*-lysosomal escape of LCN-siRNA was determined by CLSM. Cells were seeded and treated under the same conditions as above. Then, endosomes/lysosomes were labeled with LysoTracker Green DND26 (100 nM) for 1 h. After staining with DAPI, cells were imaged with a 63 × oil immersion objective under a CLSM (excitation/emission: 652/670 nm for AF647; 358/461 nm for DAPI; and 504/511 nm for LysoTracker Green DND26). In this study, at least six images (10–20 cells/image) were acquired to determine the Pearson's coefficient and the Mander's coefficient using the JaCoP plugin of ImageJ software.

2.9. Efficacy study in an in vitro inflammatory model

2.9.1. Isolation and cultivation of primary human monocytes

To obtain monocytes, blood from healthy volunteers who had not taken any medication in the previous 48 h was collected in a vacuum tube containing heparin and diluted in phosphate-buffered saline (PBS; pH 7.4). Cells were isolated by the density gradient method (using Histopaque 1077) according to the protocol described by Rios and colleagues (Rios et al., 2017), with some modifications. Cells were transferred at a density of 3×10^6 cells/mL in RPMI-1640 medium (containing 2.5% FBS) to a 24-well plate and incubated at 37 °C and 5% CO_2. After 2 h, the non-adhered cells were removed, and adhered cells (monocytes) were kept in RPMI-1640 medium for activity assays.

This procedure and experimental studies were approved by the Research Ethics Committee of the Faculty of Pharmaceutical Sciences of Ribeirão Preto (University of São Paulo, Ribeirão Preto, SP, Brazil) under the report No. 4062866. All subjects were of legal age and signed the free and informed consent form. This procedure and experimental studies were approved by the Research Ethics Committee of the School of Pharmaceutical Sciences of Ribeirao Preto (University of Sao Paulo, Ribeirao Preto, SP, Brazil) under Consubstantiated Opinion n°. 4062866. All volunteers were adult individuals, and all signed a Statement of Informed Consent.

2.9.2. In vitro inflammatory model

The ability of multifunctional LCN to reduce the amount of pro-inflammatory cytokines released into the culture medium was evaluated using cultured primary human monocytes stimulated with 1 μg/mL LPS. Formulations were used at the following concentrations: 0.05 μM free TP, naked siTNF-α or 150 nM siIL-6, LCN or LCN TP (considering 0.05 μM TP), and LCN or LCN TP with siTNF-α and/or siIL-6 150 nM.

Two experimental protocols were used. In the first protocol, cells were incubated simultaneously with LPS and the formulations for 48 h. In the second protocol, cells were stimulated with LPS for the first 24 h and then the formulations were added, maintaining culture for an additional 24 h (total 48-hours experiment). At the end of the period, the cell supernatant was removed and stored at −80 °C. In the same cells, viability was determined using the resazurin assay.

Cytokines in the supernatant, including TNF-α, IL-1β, IL-6, and transforming growth factor-beta (TGF-β), were determined using ELISA kits according to the manufacturer's recommended instructions (BD Biosciences, USA). After obtaining the data, the combination index (CI) was calculated for treatments with multifunctional LCNs (Chou, 2006). A CI < 1 indicates that the combination of drug doses has a synergistic effect beyond the simple sum of the individual effects.

2.10. Statistical analysis

All data collected were reported as means ± SD. Differences between groups were evaluated with Student's *t* test (two groups) or ANOVA with Tukey's or Dunnett's post-test for multiple comparisons. The significance level was 5% and a 95% confidence interval is reported.

3. Results

3.1. Production and characterization of LCN and LCN-hydrogel

To realize our conception, we successfully establish this platform by the top-down approach using lyotropic liquid crystal (LLC) bulk ultrasonication. Considering that the presence of additives as PAH and TP in the LCNs can affect the formed structure liquid crystalline, the physicochemical evaluations of LCNs in presence or absence of these additives were the first main of this work. Fig. 2**-A** shows under polarized light microscopy, the reverse hexagonal liquid crystalline mesophase formed by mixing MO, OA, and the aqueous phase after 24 h of equilibrium time (Fig. 2**; A**). All tested formulations showed birefringence of the fan texture (Fig. 2**; A-2 to 8**) and no mesophase transition of LCNs was observed even when TP was added (Fig. 2**; A-7 and 8**). After ultrasonication, all dispersions had a homogeneous, milky white, and opalescent macroscopic appearance. This visual appearance of the LCNs was similar to that described in the literature for various LCN systems, which is characteristic of a well-defined liquid crystalline structure, resulting in strong Rayleigh scattering to visible light, resulting in an opaque external appearance. In preliminary studies, different concentrations of PAH from 0.1 to 2.0% (w/w) were incorporated into LCNs and changed the particle size, PdI, and zeta potential, whereupon the optimal concentration of PAH in LCNs was determined to be 0.5% (w/w) (**Supplementary Table 1**). Higher concentrations of PAH negatively affected particle size and PdI, while zeta potential remained at similar levels to the 0.5% (w/w) concentration.

Briefly, DLS analysis of the hydronamic diameter and size distribution of the subsequent formulations showed that all formulations had unimodal, symmetric size distribution curves with mean size between 145 and 159 nm. The PdI ranged from 0.13 to 0.21, indicating a narrow, homogeneous particle size distribution of the LCN. The TP encapsulation efficiency of LCNs was equal to or greater than 90%. Notably, the PdI of the nanoparticles remained narrow after TP and/or siRNA loading, indicating that the nanoparticles remained uniform (Table 1).

As expected, the LCNs zeta potential was strongly affected by the addition of the positively charged polymer PAH which was from −46.8 (± 1.5) to + 11.3 (± 0.6) mV, favoring electrostatic interactions with siRNA. This interaction, at an N/P ratio of 2, resulted in a decrease in zeta potential after incubation with siRNA. In addition, the efficiency of LCNs in binding 5 μM siRNA was confirmed by the electrophoretic mobility assay (Fig. 2**; B**). Also, the addition of heparin to LCNs containing PAH and siRNA promoted the dissociation of this complex (Fig. 2**; C**), as heparin competes with siRNA for the PAH amine groups, thus releasing the siRNA without affecting its stability. The complexation of LCNs with siRNA was further validated through a RiboGreen® fluorescence-based assay, which demonstrated an efficiency greater than 99%, with no significant influence of the presence or absence of encapsulated TP.

To confirm the retention of the reverse hexagonal mesophase in the structure of LCNs after the sonication process, SAXS analysis was performed. Scattering curves with diffraction peaks in the ratio 1: $\sqrt{3}$: $\sqrt{4}$

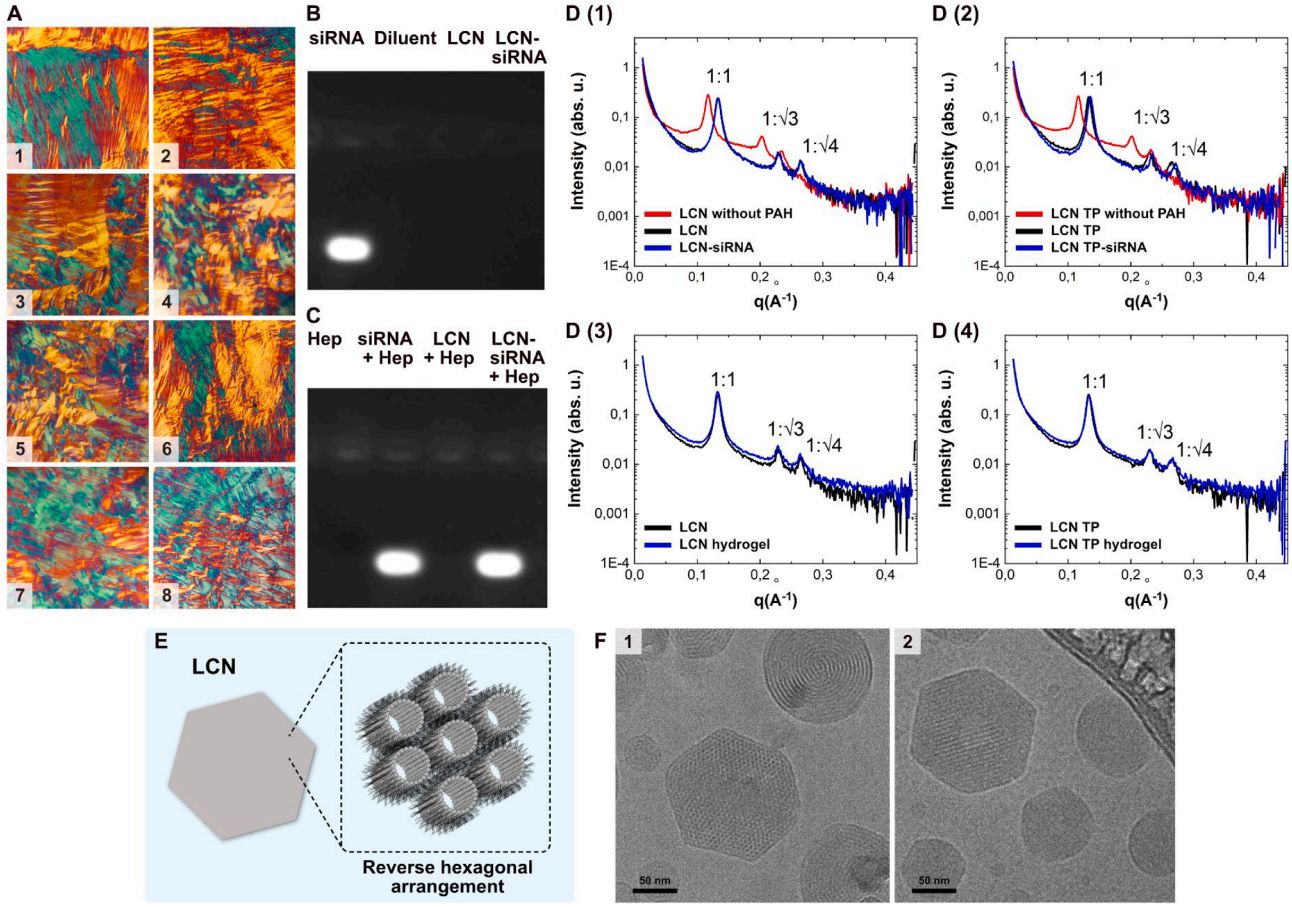

Fig. 2. Characterization of multifunctional reverse hexagonal LCN. (A) Polarized light microscopy image of the bulk hexagonal mesophase: (1) MO:OA:AP (8:1:90, w/w/w); (2–6) MO:OA:AP (8:1:90, w/w/w) with 0.1, 0.5, 1.0, 1.5 or 2.0% (w/w) of PAH polymer; (7) MO:OA:AP (8:1:90, w/w/w) with 0.04% (w/w) TP; (8) MO:OA:AP (8:1:90, w/w/w) with 0.5% (w/w) PAH and 0.04% (w/w) TP. Temperature at 25 °C and objective 32×. **(B)** Electrophoretic mobility of siRNA-loaded LCNs and **(C)** stability of siRNA released from LCN-siRNA complex following competition with heparin. **(D, 1–4)** SAXS diffractograms of LCN. The graphics show the ratio between the interplanar distances. **(E)** Schematic representation of the internal mesostructure of reverse hexagonal LCNs. **(F)** Cryo-TEM micrograph of LCNs prepared without PAH polymer (1) and with PAH polymer (2). Abbreviations: MO = monoolein; OA = oleic acid; AP = aqueous phase; PAH = poly(allylamine hydrochloride; TP = triptolide; LCNs = liquid-crystalline nanoparticles; siRNA = small interfering RNA.

Table 1
Physico-chemical properties of LCNs.

Formulation	*Z-average size (nm)*	*PdI*	*Zeta potential (mV)*	*Concentration (particles/ mL)*[a]	*TP-EE (%)*	*siRNA-EE (%)*
LCN without PAH	159.7 ± 1.1	0.13 ± 0.01	−42.9 ± 0.7	5.7 ± 0.4 × 10^{12}	n.a.	n.a.
LCN TP without PAH	145.8 ± 0.5	0.18 ± 0.01	−46.8 ± 1.5	5.4 ± 0.4 × 10^{12}	90.5 ± 5.8	n.a.
LCN	151.5 ± 1.1	0.13 ± 0.01	+11.2 ± 0.1	4.1 ± 0.2 × 10^{12}	n.a.	n.a.
LCN TP	148.3 ± 0.1	0.15 ± 0.01	+11.3 ± 0.6	4.2 ± 0.2 × 10^{12}	92.3 ± 2.5	n.a.
LCN-siRNA	155.8 ± 0.9	0.16 ± 0.01	+8.6 ± 0.5	n.a.	n.a.	99.78 ± 0.01
LCN TP-siRNA	152.8 ± 1.4	0.20 ± 0.02	+7.8 ± 0.8	n.a.	91.4 ± 3.2	99.56 ± 0.02
LCN hydrogel	156.8 ± 1.8	0.20 ± 0.04	+9.0 ± 0.8	n.a.	n.a.	n.a.
LCN TP hydrogel	155.3 ± 0.8	0.19 ± 0.02	+10.4 ± 0.5	n.a.	n.a.	n.a.
LCN-siRNA hydrogel	156.3 ± 0.8	0.21 ± 0.03	+8.0 ± 0.9	n.a.	n.a.	n.a.
LCN TP-siRNA hydrogel	158.6 ± 0.6	0.20 ± 0.02	+8.2 ± 0.5	n.a.	n.a.	n.a.

Abbreviations: TP = triptolide; LCN = liquid-crystalline nanoparticle; EE = entrapment efficiency; PAH = poly(allylamine hydrochloride); siRNA = small interfering RNA.
Data are presented by the mean ± standard deviation (n = 3).
[a] Data are presented by mean ± standard error (n = 5).

(Fig. 2; **D [1 to 4]**), corresponding to the 2D hexagonal symmetry group p6mm were obtained for all LCN (Milak and Zimmer, 2015; Silvestrini et al., 2022). The incorporation of PAH into LCNs led to an increase in the values of q ($Å^{-1}$) and the lattice parameter (Table 2), indicating a decrease in the interplanar distance between the formed reverse micelles (Amar-Yuli et al., 2007). The decrease in the lattice parameter from 6.20 to 5.50 nm ($p < 0.05$) and from 6.23 to 5.49 nm ($p < 0.05$) was observed in the presence of PAH in LCNs and LCN TP, respectively, suggesting that this hydrophilic polymer may have affected the number of water molecules available in the system and thus the dehydration process increased the mobility of the chains of MO and OA hydrocarbons, resulting in increased curvature and a concomitant decrease in the lattice parameter.

When siRNA was complexed with LCNs, a decrease in the lattice

Table 2
SAXS data and lattice parameter for the LCNs.

Formulation	*q* ($Å^{-1}$)	*Ratio*	*Mesophase symmetry*	*Mean lattice parameter (nm)*
	0.12	1:1		
LCN without PAH	0.20	1:√3	H_{II}	6.20 ± 0.04
	0.24	1:√4		
	0.12	1:1		
LCN TP without PAH	0.20	1:√3	H_{II}	6.23 ± 0.03
	0.23	1:√4		
	0.13	1:1		
LCN	0.23	1:√3	H_{II}	5.50 ± 0.02 *
	0.26	1:√4		
	0.13	1:1		
LCN TP	0.23	1:√3	H_{II}	5.49 ± 0.01 #
	0.26	1:√4		
	0.13	1:1		
LCN-siRNA	0.23	1:√3	H_{II}	5.46 ± 0.04
	0.27	1:√4		
	0.14	1:1		
LCN TP-siRNA	0.23	1:√3	H_{II}	5.36 ± 0.01 &
	0.27	1:√4		
	0.13	1:1		
LCN hydrogel	0.23	1:√3	H_{II}	5.50 ± 0.01
	0.26	1:√4		
	0.13	1:1		
LCN TP hydrogel	0.23	1:√3	H_{II}	5.45 ± 0.01
	0.27	1:√4		

Abbreviations: *q*: scattering vector; *d*: interplanar distances; α = lattice parameter; αH = mean and standard deviation of the lattice parameter; LCN = liquid-crystalline nanoparticle; PAH = poly(allylamine hydrochloride); siRNA = small interfering RNA.
Statistical analysis performed by Two-way ANOVA, Tukey post hoc test ($p < 0.05$: * = LCN without PAH *vs* LCN; # = LCN TP without PAH *vs* LCN TP; and & = LCN TP *vs* LCN TP-siRNA).

parameter was observed from 5.50 to 5.46 nm and from 5.49 to 5.36 nm for LCN TP ($p < 0.05$). This result can be explained by the attraction of siRNA molecules by the cationic PAH in the hydrophilic region, suggesting that a compaction of the hydrophilic part occurred. In contrast, when the dispersion of LCNs was incorporated into the HEC hydrogel, no change in the lattice parameter was observed, indicating that its presence did not alter the liquid crystalline structure of the LCNs, as well as their colloidal parameters.

Interestingly, when TP was added, no changes in the lattice parameters were detected, indicating that the hydrophobic TP molecule was located in the MO hydrocarbon chains or adsorbed on the surface of the reverse micelles (see scheme in Fig. 2**-E**). Moreover, the FTIR results showed that in the presence of TP in the LCN TP, the characteristic peaks of the molecule decreased, especially at the ~ 3500 cm^{-1} position corresponding to the O–H group. The peaks at 2960 and 1770 cm^{-1}, corresponding to alkyl and carbonyl group in the lactonic ring, respectively, also showed a decrease but overlapped with the characteristic peaks of the other components present in the LCNs (**supplementary Figure 1**). Additionally, the FTIR spectrum of pure MO showed characteristic peaks in ~ 3300, 2940, 1728 and 721 cm^{-1}, that could be attributed to the stretching of O–H group, CH_2 stretching, presence of C = C bonds and C–H bending. The FTIR spectrum of pure OA shows two bands at 2940 e 2856 cm^{-1} characteristics of symmetrical and asymmetrical CH_2 groups, respectively; an intense band at 1705 cm^{-1} referring to axial vibration of the carboxyl group from fatty acids (C = O), the band at 1285 cm^{-1} is attributed to the stretching the C-O group and the bands at 1460 and 940 cm^{-1} represent the O–H groups. Notably, when these compounds were combined in the LCNs, these peaks intensity was decreased due to the interaction between them for forming the internal mesostructure of LCNs. The characteristic bands of the P407 (2869 and 1110 cm^{-1}) due to C–H and C = O stretching vibration respectively, also are observed when P407 was combined in the LCNs, suggesting that a thin layer was formed externally in the LCNs. Regarding PAH, an important medium to strong band at ~ 1550 cm^{-1}, corresponding to the symmetrical angular deformation in the plane, characterizes the presence of the amine group, and this deformation is subtly shown in the nanostructures. Together, these results show that the combination of components, in the FTIR spectrum of LCNs, the functional groups remained present or with extremely slight shift, suggesting satisfactory compatibility and no evidence of interaction between the drug and the lipids and polymers of the formulation.

3.2. Stability

LCNs in the presence or absence of TP proved physically stable at room temperature and under accelerated conditions (40 °C) for approximately 30 days (Fig. 3**; A-D**). During the first 30 days, there were no significant variations in LCN size, PdI, zeta potential, and % EE-TP. However, between 30 and 90 days, a progressive increase in particle size and PdI ($p < 0.001$) was observed. This could be due to the decrease in positive charge observed after 60 days ($p < 0.01$). At a temperature of 4 °C, the physical stability of the LCNs was affected by an even shorter storage time. In the first 30 days, an increase in LCN particle size from 167.2 ± 1.4 to 178.3 ± 1.7 nm was observed, accompanied by an increase in PdI ($p < 0.01$). The zeta potential decreased rapidly with time, which could contribute to greater aggregation of the particles. Also, LCN TP showed that these parameters changed with refrigerated temperature. Probably, this phenomenon is related to the crystallization effect of MO after cooling to 4 °C (Siekmann et al., 2002).

The study of the chemical stability of TP in LCNs at room temperature showed that the amount of TP in the formulation remained constant (approximately 100%) for 90 days (Fig. 3**; E**). After 90 days, there was a significant decrease in the TP content ($p < 0.001$), mainly under accelerated conditions.

3.3. Rheological and mechanical aspects of LCN hydrogel

Evaluation of rheological behavior showed that viscosity decreased with increasing shear rate for all formulations tested, indicating non-Newtonian behavior (**Supplementary Figure 2**). To confirm these results, the rheograms were mathematically fitted using the Herschel-Bulkley model (**Supplementary Table 2**). The increased hysteresis area was obtained from hydrogels containing either LCNs or LCN TP ($p < 0.001$), reflecting a 1.5-fold increase in the thixotropic property compared to the hydrogel-only control. Although the LCN hydrogel and LCN TP hydrogel formulations showed an increase in flow behavior index (η) from 0.3 to 0.5 respectively, the pseudoplastic properties were maintained as the flow index value was<1. In addition, incorporation of LCNs into the hydrogel reflected a 1.7-fold decrease in consistency index (K) and a 3.5-fold increase in yield stress (τ_0) compared to the hydrogel-only control (Table 3).

Next, we investigated the mechanical properties of the hydrogel as they relate to the spreadability and uniformity of the formulation (Table 3). The compressive force required to deform the formulation (called compressibility) was not affected by the LCNs and was close to 0.3 N.mm. On the other hand, hydrogels containing LCNs (0.0297 ± 0.0003 N) and LCN TP (0.0313 ± 0.002 N) were found to have an increase in cohesive force compared to pure hydrogel (0.0259 ± 0.0009 N) and TP hydrogel (0.026 ± 0.001 N). Adhesive force also increased 2 to 4.2 times ($p < 0.0001$) when LCNs were incorporated. Similar results were observed in the bioadhesion test, as the force required to detach the formulation from the biological membrane increased an average of 1.2-fold for the hydrogels with the LCNs compared to the controls.

3.4. In vitro release and permeation studies

The drug release rates of LCN TP, LCN TP hydrogel, and the controls (free TP solution or TP in hydrogel without nanoparticles) were rapid within 12 h of the study (approximately 66% of the applied dose),

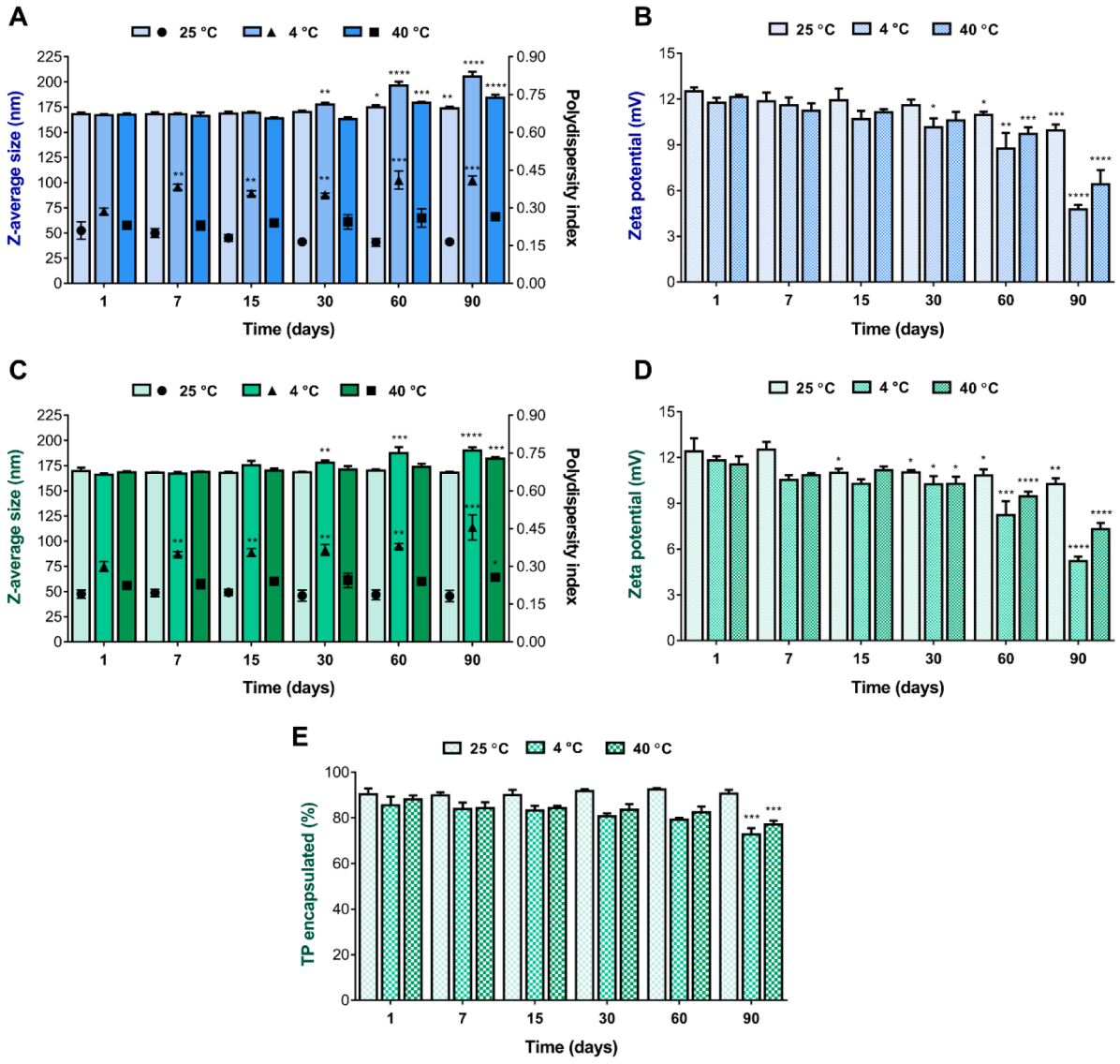

Fig. 3. Physical and chemical stability profile of LCN under different storage temperatures. Hydrodynamic diameter (z-average) and PdI of LCN **(A)** and LCN TP **(B)**. Zeta potential of LCNs **(C)** and LCN TP **(D)**. Encapsulated drug content in LCN TP **(E)**. Data shown are means ± SD (n = 3/ 3 independent formulations). Statistical analysis was determined by One-way ANOVA, Dunnet post hoc test: **** $p < 0.0001$; *** $p < 0.001$; ** $p < 0.01$ and * $p < 0.05$.

followed by sustained release from 12 to 24 h (approximately 77% of the applied dose) (**Supplementary Figure 3**). In the first hours of the TP release profile of the LCNs, a burst effect was observed compared with the control formulations, and it appears that although most of the applied TP was incorporated into the core of the nanoparticles, the free drug (approximately 10%, results from the % EE-TP assays) or the TP molecules incorporated into the outer surface of the nanoparticles were released more rapidly. This rapid release could be related to the large surface area relative to the volume of the LCN, while the continuous release could be due to the diffusion of the drugs into the hydrophobic regions of the liquid crystalline structure. The TP release kinetics in the LCN or LCN hydrogel were better fitted to the Higuchi model (amount of drug released *versus* square root of time), attributed to the particulate nature of the LCNs, while the solution followed zero-order kinetics (amount of drug released over time) (**Supplementary Table 3**).

Increasing the dispersion viscosity with the HEC polymer did not change the TP release profile but reduced the TP content permeated into the skin by 1.4 to 2.4 fold when delivered by the LCNs (Fig. 4; **A**). Furthermore, a 1.2-fold reduction in flux (*J*), 1.7-fold reduction in permeation coefficient (*P*) and a higher lag time were observed for TP delivered by the LCNs in the hydrogel compared to dispersion without hydrogel, showing greater drug interaction with the skin (Fig. 4; **B**). This greater interaction of the drug with the skin provided by the LCNs was also evidenced by a higher content retained in the SC and EP + D (Fig. 4; **C and D**). Approximately 20-fold higher concentrations ($p < 0.0001$) of TP were observed in SC (21.6 ± 1.83%, equivalent to 35.93 ± 3.05 μg/cm^2) and EP + D (46.95 ± 2.23%, equivalent to 78.23 ± 3.72 μg/cm^2) after 6 h compared with the control formulations (TP solution and TP hydrogel). At the same time, the accumulated permeate content was 3.82 ± 0.31% relative to the applied dose (6.35 ± 0.51 μg/cm^2), reflecting the increase in the retention capacity of the system. At other times, the retained content in EP + D ranged from 20 to 40% (corresponding to 33 to 52 μg/cm^2), higher than in SC, where it was 8 to 22% (corresponding to 14 to 35 μg/cm^2). In these studies, an experimental period of 6 h was chosen to evaluate the penetration depth of LCN TP using confocal microscopy (Fig. 4; **E**). In this assay, DAPI-stained nuclei appeared in blue and siRNA AF647 dye in red. The strong red fluorescence in EP + D confirmed that LCN TP was widely distributed in the skin and reached the deeper skin layers, whereas naked siRNA AF647 in SC remained superficial.

Table 3
Rheological and mechanical parameters of LCN hydrogel.

Formulation	*Hydrogel*	*Hydrogel TP*	*LCN hydrogel*	*LCN TP hydrogel*
Rheological parameters				
K (Pa.s)	6.91 ± 0.16	7.01 ± 0.11	4.05 ± 0.14 **	3.87 ± 0.53 **
τ_0 *(Pa)*	−3.87 ± 0.07	−3.96 ± 0.89	−0.90 ± 0.09 *	−1.28 ± 0.29 *
η	0.35 ± 0.03	0.32 ± 0.01	0.50 ± 0.01 *	0.51 ± 0.02 **
Thixotropy (Pa/s)	5108.5 ± 92.5	5408.3 ± 70.5	7178.7 ± 57.1 **	8032.5 ± 58.5 **
Mechanical parameters				
Cohesiveness (N)	0.026 ± 0.001	0.026 ± 0.001	0.030 ± 0.001 *	0.031 ± 0.002 *
Compressibility (N. mm)	0.292 ± 0.002	0.280 ± 0.009	0.297 ± 0.006	0.312 ± 0.005
Adhesiveness (N. mm)	0.015 ± 0.004	0.022 ± 0.001	0.039 ± 0.002 **	0.064 ± 0.003 **
Bio-adhesiveness (N.mm)	0.231 ± 0.007	0.236 ± 0.019	0.282 ± 0.014 *	0.289 ± 0.018 *

Abbreviations: TP = triptolide; LCN = liquid-crystalline nanoparticle; K = consistency index; η = flow index; and τ0 = yield stress.
Data shown are means ± SD (n = 3 for rheological parameters, cohesiveness, compressibility and adhesiveness analyzes; n = 5 for bio-adhesiveness). Statistical analysis performed by Student *t* test (** $p \leq 0.0001$ and * $p < 0.001$).

3.5. Cellular studies

Cellular biocompatibility and IC_{50} of empty LCN, LCN containing TP, and multifunctional LCN containing TP and siRNA in normal human keratinocytes determined by the resazurin fluorometry assay are summarized in Table 4.

Initially, we examined the cytotoxicity of naked siRNAs and HaCaT cells maintained maximal viability in a concentration range of naked siTNF-α or siIL-6 of 50–450 nM. The concentration of TP or PAH in the empty LCN applied to the cells was considered a crucial toxicity factor causing cellular toxicity. The presence of PAH decreased the IC_{50} of LCN by 1.3-fold with or without the drug ($p < 0.0001$) (**Supplementary Figure 3**).

The results also showed that all studied LCN containing TP had higher IC_{50} values compared to free TP. It should be emphasized that LCNs in the presence of TP and siTNF-α or siIL-6 showed a 3.8-fold increase in IC_{50} value (from 0.09 ± 0.01 to 0.34 ± 0.02 μM), and the presence of siTNF-α plus siIL-6 resulted in a 5.1-fold increase in IC_{50} (from 0.09 ± 0.01 to 0.46 ± 0.08 μM) compared to free TP ($p < 0.0001$). Interestingly, LCN complexed with siRNAs showed a slight increase in IC_{50} compared to systems without siRNA (1.3- to 1.6-fold for LCN and LCN TP, respectively). This might be related to the fact that the positive surface charge of LCNs decreases after electrostatic adsorption with siRNA.

Fig. 5 **(A)** shows the cellular internalization efficiency of HaCat cells incubated with LCN TP-siRNA. A progressive increase in internalization was observed from 1 h to 6 h, which decreased after 24 h. At all time periods examined, LCN TP promoted internalization of siRNA ($p < 0.0001$). No significant internalization was observed for naked siRNA. Visualization was performed using CLSM to support quantitative measures of internalization (Fig. 5**; B**). Nuclei stained with DAPI (blue) and surrounded by AF647 (red) were observed mainly in cells treated with LCN. Confocal microscopy of LCN TP revealed the presence of spots with prominent fluorescence signals (red) throughout the cytoplasm, in the perinuclear region, or on the cell surface. Moreover, the similarity of the fluorescence intensity of rhodamine 123 (green) between treated and untreated cells clearly indicated that morphological and structural changes (changes in mitochondrial membrane potential) were not detectable in the cells (**Supplementary Figure 5**).

To elucidate the pathways of cellular uptake, the interactions between LCN-siRNA complexes and cell membranes were studied by treating cells with various chemical endocytosis inhibitors. The cytotoxic concentrations of these inhibitors were previously examined (data not shown). These data ensure that the reduction in cellular uptake shown in Fig. 6 **(A)** is specific to the inhibitors and not to the cytotoxicity of the inhibitors. To ensure that cells were viable at the time of flow cytometry measurements, the experiment was performed in conjunction with a cell viability assay to allow measurement of both parameters (**Supplementary Figure 6**). The effect of inhibitors on LCN-siRNA uptake was measured 6 h after cell transfection and expressed as a percentage of untreated cells. Internalization of LCNs was significantly inhibited by amiloride (64.59 ± 0.89%) and cytochalasin D (62.92 ± 4.22%), sodium/proton pump inhibitors and F-actin depolarization, respectively, suggesting a macropinocytosis-mediated uptake mechanism. Furthermore, suppression of uptake was also observed for MβC (45.32 ± 3.70%) and not for filipin III (5%), suggesting a contribution of caveolin-mediated endocytosis and the involvement of flotilins [41]. Other inhibitors had no significant effect on the internalization rates of LCNs, suggesting minimal involvement of energy-dependent mechanisms, the endocytic pathway mediated by catrin, or phagocytosis.

To obtain more detailed information on the intracellular trafficking of LCNs, we performed colocalization studies with LysoTracker, a fluorescence dye commonly used to stain endosomes and lysosomes due to its acid-sensitive accumulation in these organelles. In HaCaT cells, fluorescence colocalization of siRNA labeled with AF647 (red) and endosomes/lysosomes stained with LysoTracker (green) was observed by confocal microscopy after the cells being treated with LCN siRNA at different times. Yellow-orange areas indicating colocalization of LCN siRNA in the endosomes/lysosomes were observed in the first hours of the treatments (Fig. 6**; C**). With increasing treatment duration (6 to 24 h) (Fig. 6**; C-2 and 3**), more red fluorescence was observed around the nucleus (blue), although some yellow regions were also seen. Quantitative analysis was then performed to determine the Pearson and Mander coefficients, which together indicate the precise colocalization of the pixels of each fluorescence. The Pearson r coefficient showed a stronger correlation between the 1- and 2-hour treatments (0.68 ± 0.04 and 0.638 ± 0.05, respectively) with a progressive decrease after 6 h ($p < 0.0001$). The Mander coefficients (M_1 and M_2) also indicated a high correlation in the first hours of treatment, with M_1 ranging from 0.8 to 0.6 and M_2 ranging from 0.9 to 0.7 for the treatment times of 1 and 2 h. After 6 h, the coefficients decreased significantly ($p < 0.0001$) and were 0.2 and 0.3 for M_1 and M_2, respectively, after 24 h (Fig. 6**; B**).

3.6. In vitro efficacy study

To investigate the anti-inflammatory properties of TP and two siRNAs (TNF-α and IL-6) carried by LCNs (called multifunctional LCNs), the levels of TNF-α, IL-1β, IL-6, and TGF-β1 were measured in LPS-activated primary human monocytes in two experimental protocols (Fig. 7**-A and 8-A**). Cell viability was confirmed after all treatments (**Supplementary Figure 7**). In the first experimental protocol (Fig. 7**; B-E**), simultaneous administration of TP and siTNF-α by LCNs significantly decreased the secretion of cytokines, mainly TNF-α, compared with the LPS control ($p < 0.0001$). A reduction in cytokines was also achieved by treatment with LCN TP-siIL-6. However, combining TP with siTNF-α showed a better immunomodulatory effect than the combination with siIL-6, which might be related to the complex IL-6 signaling network [42]. On the other hand, the combination of two siRNAs, siTNF-α and siIL-6, with TP drastically reduced the secretion of TNF-α (285.1 ± 13.4 pg/mL *vs* 0.5 ± 0.7 pg/mL), IL- 6 (801.3 ± 70.1 pg/mL *vs* 8.2 ± 2.5 pg/mL), IL-1β (304.0 ± 16.8 pg/mL *vs* 45.1 ± 6.6 pg/mL), and TGF-β1 (9425.0 ± 160.8 pg/mL *vs* 1982.5 ± 250.1 pg/mL) compared with the LPS control. The values found for the multifunctional treatment were equivalent to those obtained for the control (basal) cells. CI ≤ 1 for the combination of TP with siTNF-α or siIL-6 indicated a synergistic effect in reducing TNF-α and IL-6, whereas an additive effect (CI 1–1.2) was found for the other

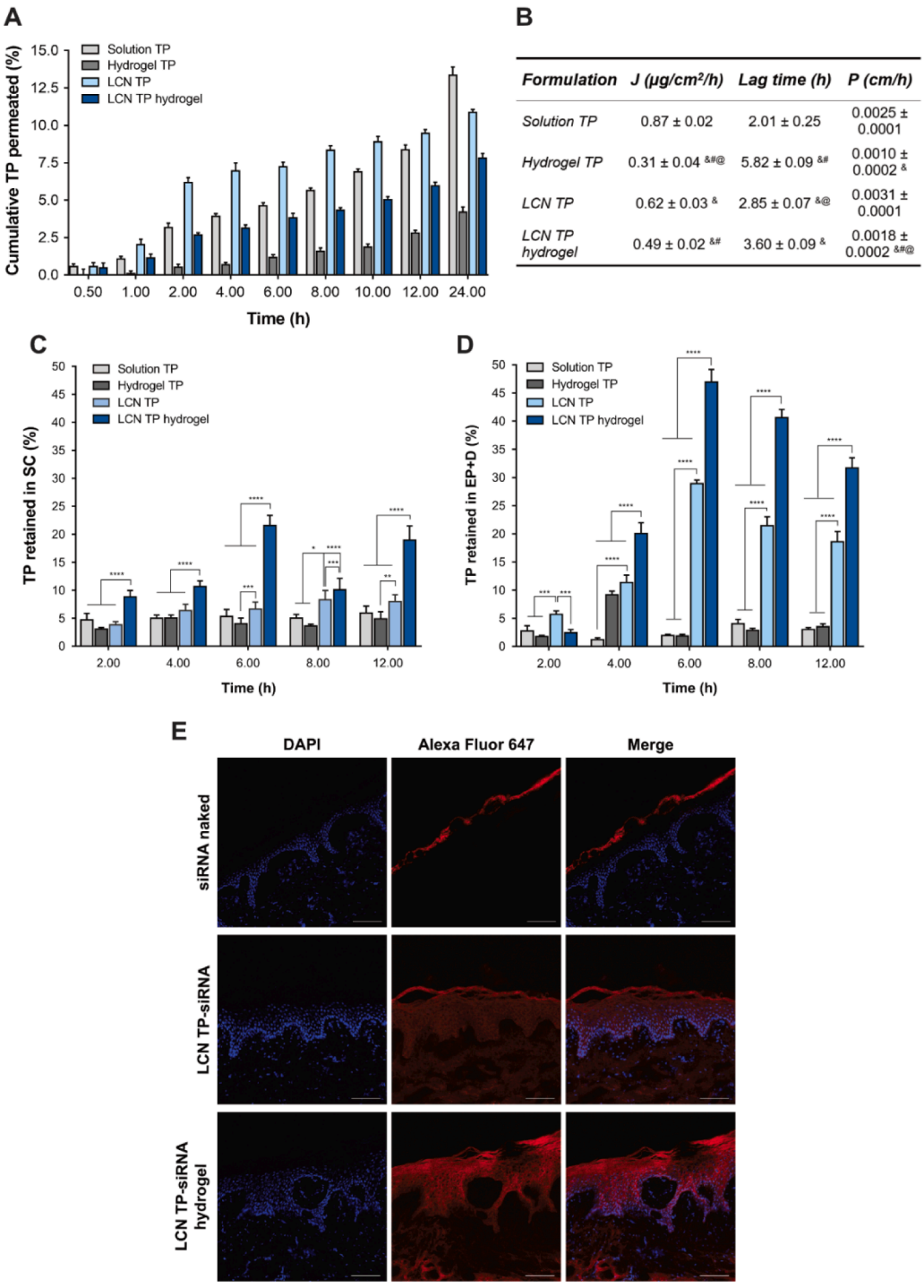

Formulation	J (μg/cm²/h)	Lag time (h)	P (cm/h)
Solution TP	0.87 ± 0.02	2.01 ± 0.25	0.0025 ± 0.0001
Hydrogel TP	0.31 ± 0.04 &#@	5.82 ± 0.09 &#	0.0010 ± 0.0002 &
LCN TP	0.62 ± 0.03 &	2.85 ± 0.07 &@	0.0031 ± 0.0001
LCN TP hydrogel	0.49 ± 0.02 &#	3.60 ± 0.09 &	0.0018 ± 0.0002 &#@

Fig. 4. ***In vitro*** **topical application of multifunctional LCNs in vertical diffusion cell. (A)** Cumulative permeated profile of TP in porcine skin. Data shown are means ± SD (n = 5). **(B)** Kinetic parameters calculated according to the permeation profile. Data shown are means ± SD (n = 5); $p < 0.0001$: "#" indicates LCN TP *vs* other formulations; "@" indicates LCN TP hydrogel *vs* other formulations; and "&" indicates solution TP *vs* other formulations (Two-way ANOVA, Tukey post hoc test). **(C-D)** TP content retained in the stratum corneum (SC) and viable epidermis + dermis (EP + D) after different times of topical application on porcine skin. Data shown are means ± SD (n = 5); **** $p < 0.0001$; *** $p < 0.001$; ** $p < 0.01$ and * $p < 0.05$ (Two-way ANOVA, Tukey post hoc test). **(E)** Representative CLSM images of porcine skin after 6 h of treatment: siRNA/siRNA-LCN TP (red - AF647) and nuclei (blue - DAPI). Scale bar corresponds to 100 μm. (For interpretation of the references to colour in this figure legend, the reader is referred to the web version of this article.)

cytokines. The combination of siTNF-α plus siIL-6 with TP, with CI ranging from 0.8 to 1, confirmed the synergy of the multi-target treatment.

Appropriate controls were performed and showed that siTNF-α or siIL-6 showed activity only when transported by LCN. On the other hand, free TP was was able to attenuate slightly the production of TNF-α, IL-1β, IL-6, and TGF-β1 compared to the LPS control ($p < 0.0001$). However, when cells were treated with TP encapsulated in LCN, this effect was more pronounced and 5.8-, 11.75-, 2.44-, and 2.57-fold inhibitions were observed for TNF-α, IL-6, IL-1 β, and TGF-β1, respectively. Interestingly, LCN (without TP or siRNAs) have been shown to modulate LPS-stimulated cytokine secretion to a lesser extent due to their lipid content, mainly OA.

Finally, we investigated whether multifunctional LCNs were able to knockdown the cytokines production by LPS-stimulated cells. Multifunctional LCNs significantly inhibited cytokine secretion ($p < 0.0001$), as shown in Fig. 8 **(B-E)**. A significant effect was observed for TNF-α, with an 11.4-fold decrease compared with LPS control, and a CI of approximately 1 suggests moderate synergism with co-administration of TP and siTNF-α plus siIL-6 by LCNs. For the other cytokines, IL-1β, IL-6, and TGF-β, there were a 2.63-, 3.88-, and 4.1-fold decreases, respectively, compared with the LPS control. The CI of 1 to 1.2 suggests an additional effect of multifunctional treatment on these cytokines. In this experimental protocol, we again observed that the combination of TP

Table 4
IC_{50} values for LCN and controls in cytocompatibility assay in keratinocytes HaCaT lineage.

Sample	*IC_{50} values*		
	Particle/ mL (10^8)	*Molarity of TP (μM)*	*Molarity of siRNA (nM)*
TP free	n.a.	0.09 ± 0.01	n.a.
siTNF-α naked	n.a.	n.a.	n.d.
siIL-6 naked	n.a.	n.a.	n.d.
LCN without PAH	3.23 ± 0.09	n.a.	n.a.
LCN TP without PAH	1.51 ± 0.15	0.26 ± 0.02 #	n.a.
LCN	2.28 ± 0.07	n.a.	n.a.
LCN TP	1.19 ± 0.08	0.26 ± 0.01 *#	n.a.
LCN-siTNF-α	3.19 ± 0.12	n.a.	210.0 ± 11.0
LCN TP-siTNF-α	1.91 ± 0.11	0.34 ± 0.02 #	197.0 ± 12.0
LCN-siIL-6	3.11 ± 0.26	n.a.	204.3 ± 9.5
LCN TP-siIL-6	1.92 ± 0.23	0.35 ± 0.05 #	198.8 ± 6.7
LCN-siTNF-α + siIL-6	3.68 ± 0.18	n.a.	249.0 ± 14.0
LCN TP- siTNF-α + siIL-6	2.59 ± 0.27	0.46 ± 0.08 #	267.1 ± 9.7

Abbreviations: TP = triptolide; LCN = liquid-crystalline nanoparticle; PAH = poly(allylamine hydrochloride); siRNA = small interfering RNA; TNF-α = tumor necrosis factor-alpha; IL-6 = interleukine-6; n.a. = not applicable; n.d. = not determined.
Data are presented by the mean ± SD (n = 8). Statistical analysis performed by Two-way ANOVA, Tukey post hoc test (p = 0.0001: * LCN without PAH compared with LCN; # = groups compared with free TP).

with siTNF-α had stronger effects than the combination with siIL-6, but the multi-target treatment provided greater suppression of cytokine production. Treatment with controls, including free TP, LCN TP, LCN with or without siTNF-α or siIL-6, showed less pronounced effects on IL-1β and IL-6 secretion ($p < 0.001$) in contrast to that observed for TNF-α and TGF-β ($p < 0.0001$).

4. Discussion

Safe and efficient design of multifunctional nanoparticles for co-administration of drugs and nucleic acids is an emerging requirement to achieve improved therapeutic effects, especially in psoriasis (Ahamad et al., 2021). One of the major challenges is to deliver the drugs to the deeper layers of the skin where inflammation occurs. In the present study, we report for the first time the development and characterization of LCNs loaded with TP and their surface modified with the cationic polymer PAH to allow electrostatic adsorption of siRNA molecules targeting TNF-α and IL-6. These multifunctional LCNs showed appropriate physicochemical properties for topical application, in addition to excellent skin penetration and gene release ability.

The LCNs developed in this work have negative residual charges related to the components of the formulation, such as MO and OA, and therefore modifications to the outer surface of the particles are necessary to overcome this disadvantage and favor the electrostatic interaction of siRNAs. Previous studies by our research group have focused on the use of PEI polymer as a residual charge modifier for nanoparticles and have been successful. Moreover, PEI amounts of 1% or more were necessary to induce a slight residual positive charge to the system, which may have been the reason for the high polydispersion rates found at that time (Depieri et al., 2016; Petrilli et al., 2016; Tofani et al., 2018). However, this polymer is highly toxic, and the biocompatibility of cationic polymers for long-term use remains a critical obstacle that needs to be addressed for *in vivo* use (Caillaud et al., 2020; Yan et al., 2022).

Given the advantages of using the polymer PAH, namely high efficiency of cellular uptake, pH-dependent control of drug release, and better cytocompatibility compared with other cationic polyelectrolytes (diallyl dimethyl ammonium chloride and PEI) (Di Silvio et al., 2019; Han et al., 2015; Wang et al., 2012, 2015; Zhao et al., 2012), our first objective as an innovative step for the production of LCNs and overcome the previous existing limitations was to find the appropriate concentration of PAH to achieve a positive surface charge and] to obtain the reverse hexagonal liquid crystal structure of LCN. We chose a concentration of 0.5% (PAH) because it did not affect the size of the particles, which was about 150 nm with a monomodal size distribution and a positive zeta potential. Furthermore, PAH did not change the reverse hexagonal pattern of LCNs (confirmed by polarized light microscopy, SAXS and cryo-TEM), unlike other polyelectrolytes (PEI, oleylamine and DOTAP) reported in the literature (Astolfi et al., 2017; Kim and Leal, 2015; Petrilli et al., 2016).

Moreover, an excellent compatibility between the components of the formulation was confirmed, and the incorporation of PAH did not alter this previously recognized pattern (Kaul et al., 2022; Thapa et al., 2015). We also, show that the location of PAH in LCNs, at the hydrophilic interface of the reverse micelles of the reverse hexagonal structure, favored the encapsulation of the drug in hydrophobic domains and decreased the water channels (decreased lattice parameter and displacement of the scattering vector), between micelles forming the reverse hexagonal mesophase. In addition to these results, the cationic LCNs stored at room temperature showed colloidal and chemical stability, which according to the literature is due to the presence and interactions of P407 with the LLC structure (Amar-Yuli et al., 2007; Silvestrini et al., 2020). Furthermore, it is suggested that the mobile and immobile molecular segments of PAH on the surface of the nanoparticles may additionally contribute to the electrosteric stability (Himmelstoß and Hirsch, 2019; Zhang et al., 2017).

Our next objective was to evaluate the efficiency of LCNs in delivering TP in high concentration and retaining the drug in the skin layer of interest (epidermis). This drug is known for its potent anti-inflammatory activity, but its low skin permeabilityand high toxicity limit its therapeutic use (Tong et al., 2021; Yang et al., 2017). In our work, the proposed LCNs showed high loading efficiency (>90%), and both LCN TP and LCN TP in hydrogel exhibited a drug release profile adapted to the Higuchi model, which was favorable for this proposed work. We hypothesize that this behavior is related to the lipid composition of LCNs and the hydrophobic character of TP, which allows unfavorable distribution in the lipid phase of LCNs and consequently sustained release. Moreover, the presence of OA in the LCNs may also affect the diffusion rate of the drug, since it is already known that OA alters the lattice parameter of the liquid crystalline structures, leading to a change in the degree of tortuosity and the orientation of the water channels (Gabr et al., 2017; Milak and Zimmer, 2015). Such properties also affect the interaction with biological membranes. When applied to biological membranes such as porcine ear skin, the developed LCNs were able to accumulate TP in the deeper layers of the skin, followed by low permeate content through the skin. This effect is attributed to the emulsifying capacity of the components of the lipid matrix, resulting from the hydrolysis of MO into OA and glycerin, increasing skin hydration and disorganizing the SC (Lopes et al., 2007). Surprisingly, the LCN TP hydrogel increased the amount of TP retained in the viable epidermis and dermis and decreased the flux and the permeation coefficient. This can be attributed to the non-Newtonian pseudoplastic character and the rheological properties of the hydrogel formed with the LCNs, such as greater bioadhesiveness and flow resistance (Lee et al., 2009; Nunes et al., 2016).

In addition to targeted delivery to the disease site, biocompatibility and efficient cellular delivery should be investigated. We have confirmed that LCNs have good cytocompatibility in HaCaT keratinocyte cell line, one of the major resident skin cells involved in the development of psoriasis. We demonstrated that LCNs attenuated the toxic effects of free TP, similar to what Zhang and colleagues (2018) (Zhang et al., 2018) observed. In addition, cell viability was increased when cells were treated with multifunctional LCN (TP, siTNF-α and siIL-6), which may be due to reduced residual positive charge of complexed LCNs. We also observed that cells treated with bicompatible LCN

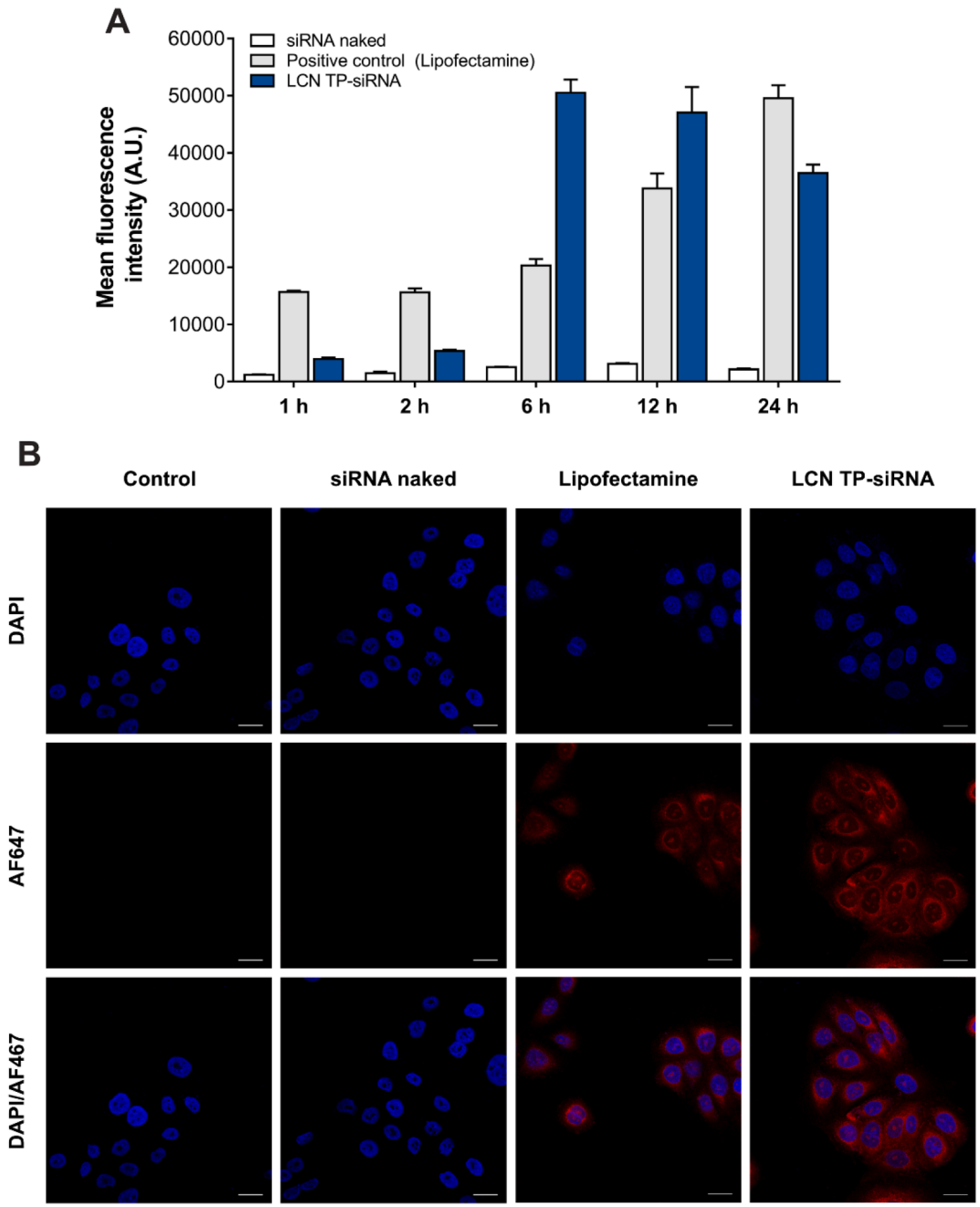

Fig. 5. Cell internalization of LCN-siRNA. (A) Cell internalization measured by flow cytometry at different treatment times. Data shown are means ± SD (n = 4). **(B)** Representative CLSM images after 6 h of treatment. Nuclei (blue – DAPI) and siRNA/LCN (red – AF647). Scale bar corresponds to 20 μm. (For interpretation of the references to colour in this figure legend, the reader is referred to the web version of this article.)

concentrations did not exhibit morphological or structural changes, which is consistent with the biocompatible profile of PAH and the lipid components of LCNs (Di Silvio et al., 2019; Tan et al., 2019; Wang et al., 2015). Therefore, it is of great importance to have a balance between surface charge and cytotoxicity. Maintaining a positive charge on the surface of nanoparticles is important to ensure siRNA loading and efficient entry into cells. Our results show rapid absorption, with a maximum at 6 h after incubation with the LCNs.

Motivated by the rapid and high uptake of LCNs, we decided to investigate possible mechanisms involved in the process of endocytic uptake. Depending on the cell type and the physicochemical properties of the nanomaterials different mechanisms may be involved in nanoparticle uptake (Makvandi et al., 2021; Tan et al., 2019). Pretreatment with different chemical endocytic inhibitors showed that cellular uptake of LCNs was significantly reduced by amiloride or cytochalasin D, inhibitors attributed to the macropinocytosis pathway, and that an active influence of caveolin-mediated endocytosis was demonstrated due to significant inhibition by MβC. Such results are in agreement with PAH-modified nanoparticles and malleable nanoparticles reported previously (Andreozzi et al., 2017; Jagielski et al., 2021; Rodrigues et al., 2019; Tan et al., 2019). Other mechanisms such as fusion with the lipid bilayer and the influence of the hexagonal structure have also been proposed as factors enabling rapid uptake of these LCNs into cells (Dyett et al., 2019; Rodrigues et al., 2019). In addition to this efficient uptake ability, there are hypotheses that cubic or reverse hexagonal LCNs have fusogenic properties that lead to the formation of pores in the endolysosomal membrane favoring the delivery of drugs ans nucleic acid (Kim and Leal, 2015; Leal et al., 2010). Consistent with the literature, we observed

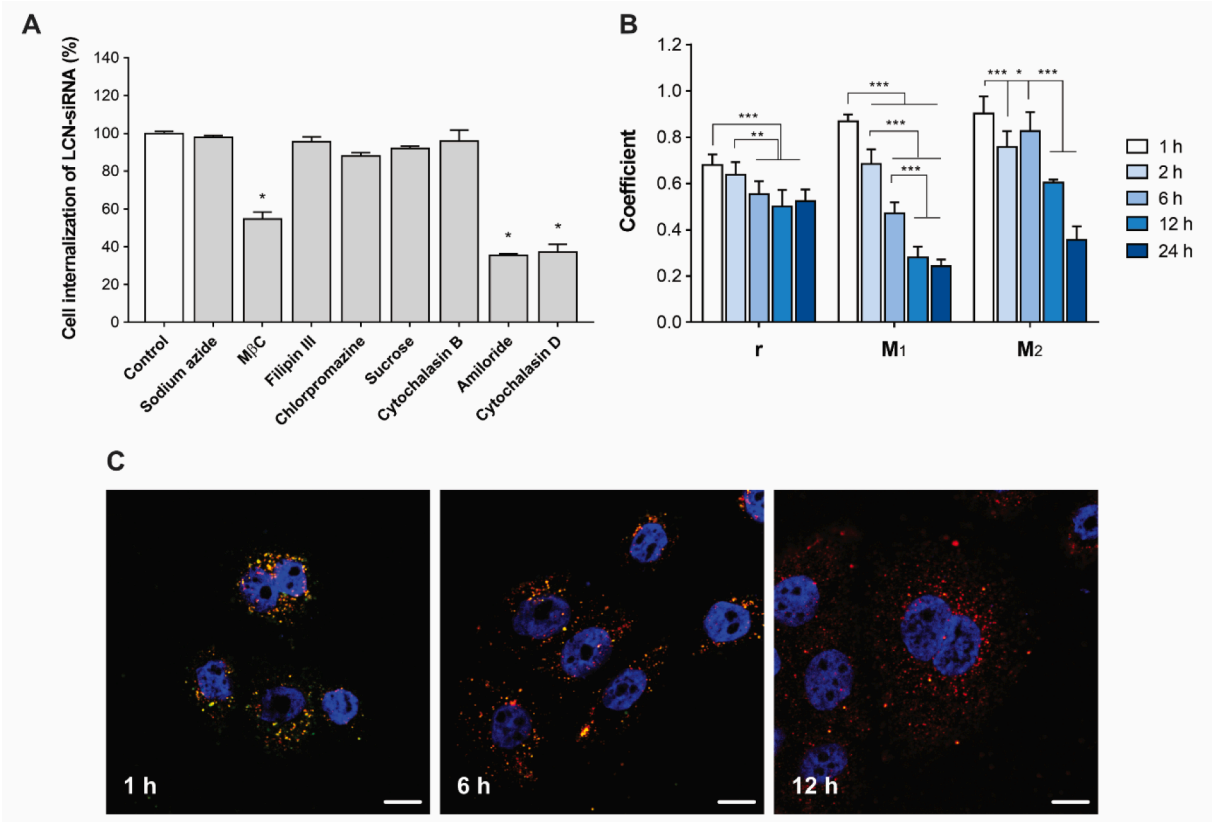

Fig. 6. Intracellular trafficking of LCN-siRNA. (A) Internalization of LCN-siRNA in the presence of endocytosis inhibitors: sodium azide (energy dependent processes), MβC and filipin III (caveolae-mediated endocytosis), chlorpromazine and sucrose (clathrin-mediated endocytosis), cytochalasin B (phagocytosis), amiloride and cytochalasin D (macropinocytosis). Data shown are means ± SD (n = 4); * $p < 0.0001$ (Student's t test). **(B)** Pearson's coefficient (r) and Mander's coefficients (M_1 and M_2) calculated between red (AF647) and green (Lysotracker Green DND26) signals. Data shown are means ± SD (n = 6/3 independent tests); * $p < 0.05$; ** $p \leq 0.001$; and *** $p < 0.0001$ (Two-Way ANOVA, Tukey post hoc test). **(C)** Representative CLSM images of intracellular trafficking of LCNs after 1, 6 and 12 h of treatment. siRNA-LCN (red – AF647), *endo*-lysosomes (green – Lysotracker Green DND26), nuclei (blue – DAPI). Images with 25 × magnification of the original. Scale bar corresponds to 10 μm. (For interpretation of the references to colour in this figure legend, the reader is referred to the web version of this article.)

endo-lysosomal escape over time in our co-location studies.

Finally, after confirming the efficient cellular internalization of LCNs, we demonstrated the immunomodulatory effects of the simultaneous administration of TP, siTNF-α, and siIL-6 by LCNs in LPS-stimulated cells. TNF-α and IL-6 are therapeutic targets that have been extensively studied in antisense therapy of anti-inflammatory diseases (Gürcan et al., 2021; Lee et al., 2022, 2020; Rosa et al., 2018; Suzuki et al., 2021; Viegas et al., 2020). However, co-administration with TP with the aim of achieving a synergistic effect in the treatment of psoriasis remains an innovative strategy to date. We demonstrated that multifunctional treatment with LCNs resulted in a significant reduction of TNF-α, IL-1β, IL-6, and TGF-β1 released by LPS-stimulated cells. As a natural compound, the anti-inflammatory effect of TP is noteworthy. There is evidence that TP modulates various signaling pathways and inhibits the activation of Toll-like receptors, resulting in a reduction of pro-inflammatory mediators in macrophages and other cells of the immune system (Tong et al., 2021; Yuan et al., 2019). Still, when transported by LCNs and combined with siTNF-α and siIL-6, these effects were even more pronounced. TNF-α is a cytokine that is instrumental in signaling, activation, and amplification of the psoriasis immune cascade. IL-6 and IL-1β are associated with the IL-23/Th17 axis and regulate pro-inflammatory mediators, T-cell differentiation, and epidermal proliferation (Armstrong and Read, 2020; Schön, 2019). In addition to the cytokines mentioned above, other cytokines such as TGF-β1 have also been associated with the severity of psoriatic lesions (Han et al., 2010). Therefore, it is of great importance to maintain these cytokines at baseline levels to reduce pro-inflammatory signaling and psoriasis score.

Overall, our study clearly demonstrated that the preparation of LCNs with biocompatible lipids and PAH is an ideal platform to overcome the limitations of cutaneous delivery of TP and free siRNAs. The combination of these two therapeutic agents in LCNs is a potential strategy to improve topical treatment of psoriasis and other inflammatory diseases.

5. Conclusion

By identifying the challenges in the dermal delivery of TP and siRNA, we have developed an innovative multifunctional nanoparticle based on lyotropic liquid crystal technology that overcomes various extracellular/intracellular barriers to promote bioavailability and achieve better therapeutic effects. This is compelling evidence that LCNs are efficient platforms to incorporate drugs and to enable surface chemical modifications to deliver genes. Significatively, we have shown that the developed LCNs have satisfactory colloidal properties for dermal drug and nucleic acid delivery, long-term stability, satisfactory rheological properties with incorporation of the dispersion into the HEC hydrogel, and better drug release profile in the deeper layers of the skin, which is essential to obtain local therapeutic effects and avoid adverse conditions. At the cellular level, LCNs showed cytocompatibility, cellular release efficiency, and endo/lysosomal escape. Equally important, LCNs successfully co-administered three therapeutic agents (TP, siTNF-α, and siIL-6), which together had a significantly greater synergistic effect on downregulation of pro-inflammatory cytokines in LPS-stimulated cells than when these drugs were administered individually.

Taken together, the results reported in this report provide a solid foundation that LCNs containing TP, siTNF-α and siIL-6 have the potential to suppress multiple targets of inflammation in psoriasis and

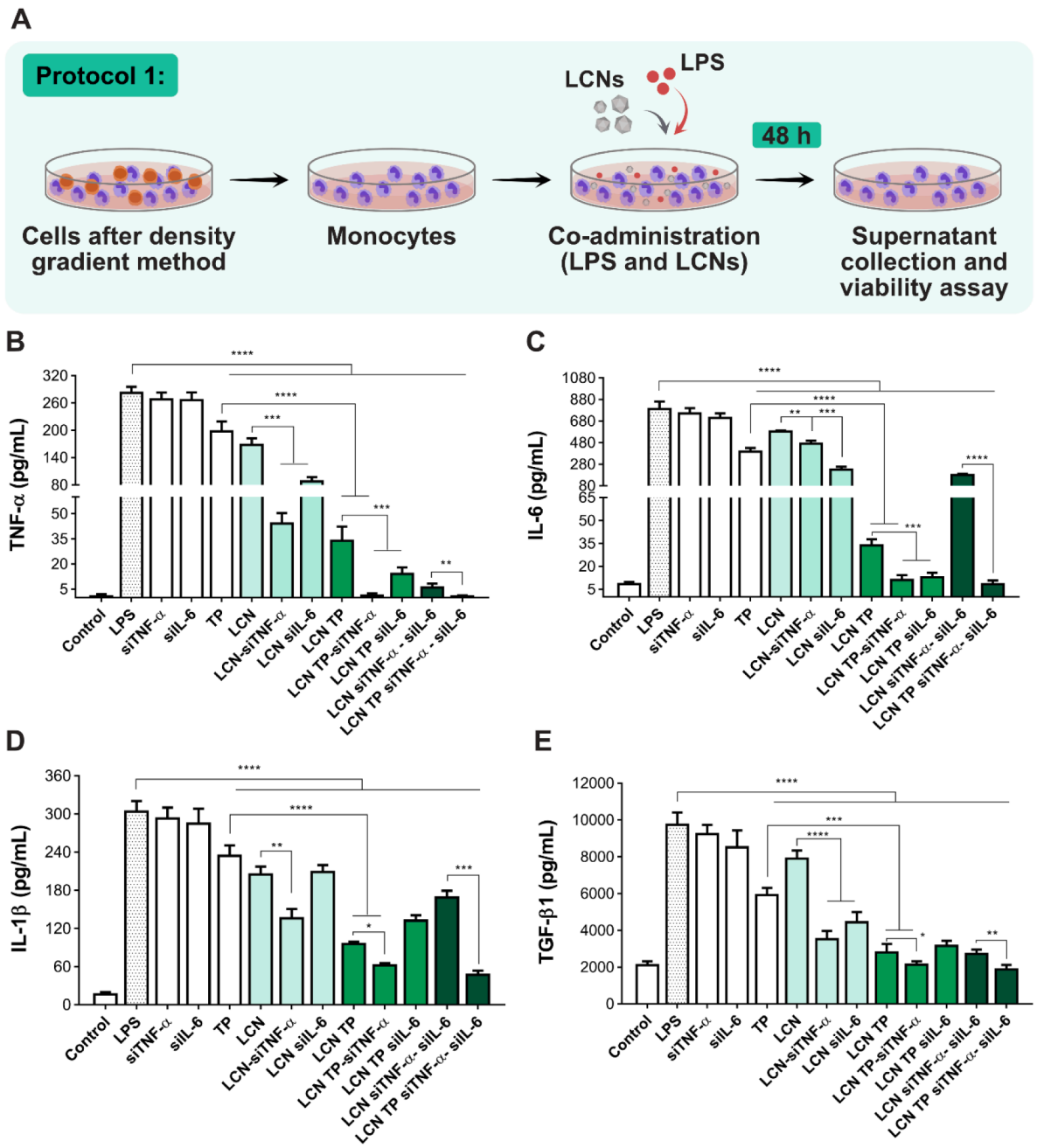

Fig. 7. Cytokine production in primary human monocytes cells stimulated with LPS and treated with the formulations for 48 h. (A) Graphical representation of protocol for evaluating therapeutic efficacy. Levels of TNF-α **(B)**, IL-1β **(C)**, IL-6 **(D)** and TGF-β1 **(E)** secreted by cells. RPMI-1640 culture medium (containing 2.5% FBS) and LPS (1 μg/ mL) were used as negative control and positive control, respectively. Data shown are means ± SD (n = 3/ 3 independent tests); Two way-ANOVA, Tukey's post test: * $p < 0.05$; ** $p < 0.01$; *** $p < 0.001$ and **** $p < 0.0001$.

other inflammatory skin diseases, stimulating preclinical investigations and large-scale production studies. In addition, the developed LCNs can also be applied as a platform for the co-delivery of other drugs and nucleic acids targeting skin diseases that aim to regulate multi-targets in their pathology.

Data availability

All of the data reported in this work are available upon request.

CRediT authorship contribution statement

Ana Vitória Pupo Silvestrini: Conceptualization, Investigation, Methodology, Software, Validation, Formal analysis, Writing – original draft. **Fabíola Garcia Praça:** Methodology, Software, Validation. **Marcel Nani Leite:** Methodology, Software, Validation. **Márcia Carvalho de Abreu Fantini:** Methodology, Software. **Marco Andrey Cipriani Frade:** Methodology, Software, Resources. **Maria Vitória Lopes Badra Bentley:** Conceptualization, Resources, Writing – review & editing, Supervision, Project administration, Funding acquisition.

Declaration of Competing Interest

The authors declare that they have no known competing financial interests or personal relationships that could have appeared to influence the work reported in this paper.

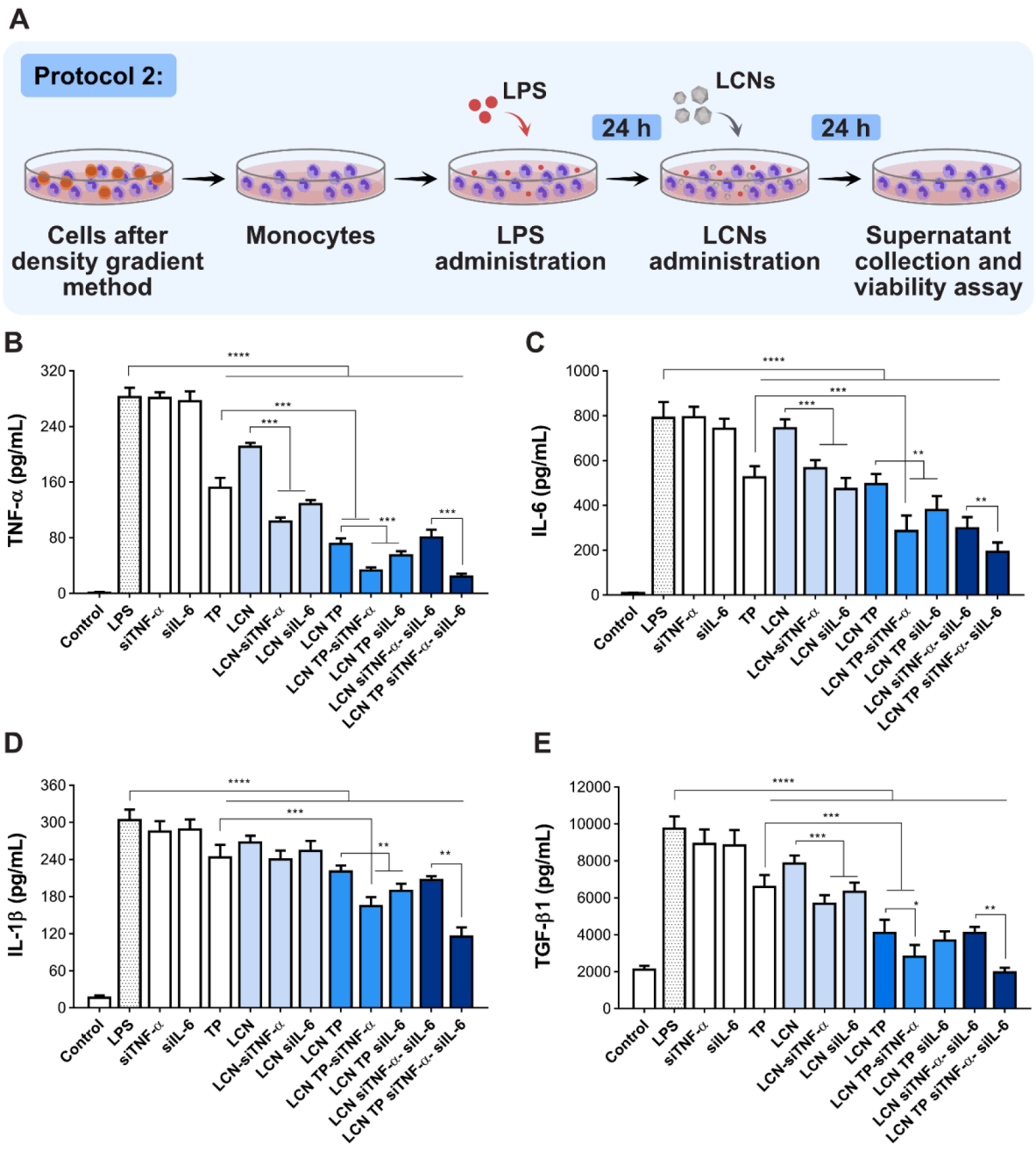

Fig. 8. Cytokine production in primary human monocytes cells pre-stimulated with LPS for 24 h, followed by treatments for another 24 h. (A) Graphical representation of protocol for evaluating therapeutic efficacy. Levels of TNF-α **(B)**, IL-1β **(C)**, IL-6 **(D)** and TGF-β1 **(E)** secreted by cells. RPMI-1640 culture medium (containing 2.5% FBS) and LPS (1 μg/ mL) were used as negative control and positive control, respectively. Data shown are means ± SD (n = 3/ 3 independent tests); Two way-ANOVA, Tukey's post test: * $p < 0.05$; ** $p < 0.01$; *** $p < 0.001$ and **** $p < 0.0001$.

Data availability

No data was used for the research described in the article.

Acknowledgements

This work was developed within the framework of National Institute of Science and Technology of Pharmaceutical Nanotechnology (INCT-Nanofarma), and supported by São Paulo Research Foundation (FAPESP, Brazil, grant #2014/50928-2) and "Conselho Nacional de Desenvolvimento Científico e Tecnológico" (CNPq, Brazil, grant #465687/2014-8). A.V.P.S. was fellowship of FAPESP (grant #2018/08253-9). The author thanks Dr. Osvaldo de Freitas and Dr. Maíra Peres Ferreira Duarte for the accessibility in using the equipment for rheological and textural analysis.

The authors would like to thank LNNano/CNPEM for the access to the electron microscopy facility and technical support in the execution of the proposal TEM20210538. The authors also thank the Multiuser Facility of the GFCx-Instituto de Física-USP, for the SAXS measurements.

Appendix A. Supplementary data

Supplementary data to this article can be found online at https://doi.org/10.1016/j.ijpharm.2023.123019.

References

Ahamad, N., Kar, A., Mehta, S., Dewani, M., Ravichandran, V., Bhardwaj, P., Sharma, S., Banerjee, R., 2021. Immunomodulatory nanosystems for treating inflammatory diseases. Biomaterials 274, 120875. https://doi.org/10.1016/j.biomaterials.2021.120875.

Amar-Yuli, I., Wachtel, E., Shoshan, E.B., Danino, D., Aserin, A., Garti, N., 2007. Hexosome and hexagonal phases mediated by hydration and polymeric stabilizer. Langmuir 23, 3637–3645. https://doi.org/10.1021/la062851b.

Andreozzi, P., Diamanti, E., Py-Daniel, K.R., Cáceres-Vélez, P.R., Martinelli, C., Politakos, N., Escobar, A., Muzi-Falconi, M., Azevedo, R., Moya, S.E., 2017. Exploring the pH Sensitivity of Poly(allylamine) Phosphate Supramolecular Nanocarriers for Intracellular siRNA Delivery. ACS Appl. Mater. Interfaces 9, 38242–38254. https://doi.org/10.1021/acsami.7b11132.

Armstrong, A.W., Read, C., 2020. Pathophysiology, Clinical Presentation, and Treatment of Psoriasis. JAMA 323, 1945. https://doi.org/10.1001/jama.2020.4006.

Astolfi, P., Giorgini, E., Gambini, V., Rossi, B., Vaccari, L., Vita, F., Francescangeli, O., Marchini, C., Pisani, M., 2017. Lyotropic Liquid-Crystalline Nanosystems as Drug Delivery Agents for 5-Fluorouracil: Structure and Cytotoxicity. Langmuir 33, 12369–12378. https://doi.org/10.1021/acs.langmuir.7b03173.

Boakye, C.H.A., Patel, K., Doddapaneni, R., Bagde, A., Marepally, S., Singh, M., 2017. Novel amphiphilic lipid augments the co-delivery of erlotinib and IL36 siRNA into the skin for psoriasis treatment. J. Control. Release 246, 120–132. https://doi.org/10.1016/j.jconrel.2016.05.017.

Caillaud, M., El Madani, M., Massaad-Massade, L., 2020. Small interfering RNA from the lab discovery to patients' recovery. J. Control. Release 321, 616–628. https://doi.org/10.1016/j.jconrel.2020.02.032.

Campos, P.M., Praça, F.G., Mussi, S.V., Figueiredo, S.A., Fantini, M.C.d.A., Fonseca, M.J.V., Torchilin, V.P., Bentley, M.V.L.B., 2020. Liquid crystalline nanodispersion functionalized with cell-penetrating peptides improves skin penetration and anti-inflammatory effect of lipoic acid after in vivo skin exposure to UVB radiation. Drug Deliv. Transl. Res. 10 (6), 1810–1828. https://doi.org/10.1007/s13346-020-00840-2.

Chou, T.-C., 2006. Theoretical Basis, Experimental Design, and Computerized Simulation of Synergism and Antagonism in Drug Combination Studies. Pharmacol. Rev. 58, 621–681. https://doi.org/10.1124/pr.58.3.10.

Depieri, L.V., Borgheti-Cardoso, L.N., Campos, P.M., Otaguiri, K.K., De Carvalho Vicentini, F.T.M., Lopes, L.B., Fonseca, M.J.V., Bentley, M.V.L.B., 2016. RNAi mediated IL-6 in vitro knockdown in psoriasis skin model with topical siRNA delivery system based on liquid crystalline phase. Eur. J. Pharm. Biopharm. 105, 50–58. https://doi.org/10.1016/j.ejpb.2016.05.012.

Di Silvio, D., Martínez-Moro, M., Salvador, C., de los Angeles Ramirez, M., Caceres-Velez, P.R., Ortore, M.G., Dupin, D., Andreozzi, P., Moya, S.E., 2019. Self-assembly of poly(allylamine)/siRNA nanoparticles, their intracellular fate and siRNA delivery. J. Colloid Interface Sci. 557, 757–766. https://doi.org/10.1016/j.jcis.2019.09.082.

Dyett, B.P., Yu, H., Strachan, J., Drummond, C.J., Conn, C.E., 2019. Fusion dynamics of cubosome nanocarriers with model cell membranes. Nat. Commun. 10, 4492. https://doi.org/10.1038/s41467-019-12508-8.

Gabr, M.M., Mortada, S.M., Sallam, M.A., 2017. Hexagonal Liquid Crystalline Nanodispersions Proven Superiority for Enhanced Oral Delivery of Rosuvastatin. In Vitro Characterization and In Vivo Pharmacokinetic Study. J. Pharm. Sci. 106, 3103–3112. https://doi.org/10.1016/j.xphs.2017.04.060.

Gürcan, S., Tsapis, N., Reynaud, F., Denis, S., Vergnaud, J., Özer, Ö., Fattal, E., 2021. Combining dexamethasone and TNF-α siRNA within the same nanoparticles to enhance anti-inflammatory effect. Int. J. Pharm. 598, 120381. https://doi.org/10.1016/j.ijpharm.2021.120381.

Han, L., Tang, C., Yin, C., 2015. Dual-targeting and pH/redox-responsive multi-layered nanocomplexes for smart co-delivery of doxorubicin and siRNA. Biomaterials 60, 42–52. https://doi.org/10.1016/j.biomaterials.2015.05.001.

Han, G., Williams, C.A., Salter, K., Garl, P.J., Li, A.G., Wang, X.-J., 2010. A Role for TGFβ Signaling in the Pathogenesis of Psoriasis. J. Invest. Dermatol. 130, 371–377. https://doi.org/10.1038/jid.2009.252.

Hawkes, J.E., Chan, T.C., Krueger, J.G., 2017. Psoriasis pathogenesis and the development of novel targeted immune therapies. J. Allergy Clin. Immunol. 140, 645–653. https://doi.org/10.1016/j.jaci.2017.07.004.

Himmelstoß, S.F., Hirsch, T., 2019. Long-Term Colloidal and Chemical Stability in Aqueous Media of NaYF 4 -Type Upconversion Nanoparticles Modified by Ligand-Exchange. Part. Part. Syst. Charact. 36, 1900235. https://doi.org/10.1002/ppsc.201900235.

Jagielski, J., Przysiecka, Ł., Flak, D., Diak, M., Pietralik-Molińska, Z., Kozak, M., Jurga, S., Nowaczyk, G., 2021. Comprehensive and comparative studies on nanocytotoxicity of glyceryl monooleate- and phytantriol-based lipid liquid crystalline nanoparticles. J. Nanobiotechnology 19, 1–18. https://doi.org/10.1186/s12951-021-00913-5.

Karimi, M., Ghasemi, A., Sahandi Zangabad, P., Rahighi, R., Moosavi Basri, S.M., Mirshekari, H., Amiri, M., Shafaei Pishabad, Z., Aslani, A., Bozorgomid, M., Ghosh, D., Beyzavi, A., Vaseghi, A., Aref, A.R., Haghani, L., Bahrami, S., Hamblin, M. R., 2016. Smart micro/nanoparticles in stimulus-responsive drug/gene delivery systems. Chem. Soc. Rev. 45, 1457–1501. https://doi.org/10.1039/C5CS00798D.

Kaul, S., Nagaich, U., Verma, N., 2022. Preclinical assessment of nanostructured liquid crystalline particles for the management of bacterial keratitis: in vivo and pharmacokinetics study. Drug Deliv Transl. Res. 12 (7), 1719–1737. https://doi.org/10.1007/s13346-021-01072-8.

Kim, H., Leal, C., 2015. Cuboplexes: Topologically Active siRNA Delivery. ACS Nano 9, 10214–10226. https://doi.org/10.1021/acsnano.5b03902.

Kim, B., Park, J., Sailor, M.J., 2019. Rekindling RNAi Therapy: Materials Design Requirements for In Vivo siRNA Delivery. Adv. Mater. 31, 1903637. https://doi.org/10.1002/adma.201903637.

Leal, C., Bouxsein, N.F., Ewert, K.K., Safinya, C.R., 2010. Highly Efficient Gene Silencing Activity of siRNA Embedded in a Nanostructured Gyroid Cubic Lipid Matrix. J. Am. Chem. Soc. 132, 16841–16847. https://doi.org/10.1021/ja1059763.

Lee, W.-R., Lin, Y.-K., Alalaiwe, A., Wang, P.-W., Liu, P.-Y., Fang, J.-Y., 2020. Fractional Laser-Mediated siRNA Delivery for Mitigating Psoriasis-like Lesions via IL-6 Silencing. Mol. Ther. - Nucleic Acids 19, 240–251. https://doi.org/10.1016/j.omtn.2019.11.013.

Lee, W.-R., Chou, W.-L., Lin, Z.-C., Sung, C.T., Lin, C.-Y., Fang, J.-Y., 2022. Laser-assisted nanocarrier delivery to achieve cutaneous siRNA targeting for attenuating psoriasiform dermatitis. J. Control. Release 347, 590–606. https://doi.org/10.1016/j.jconrel.2022.05.032.

Lee, C.H., Moturi, V., Lee, Y., 2009. Thixotropic property in pharmaceutical formulations. J. Control. Release 136, 88–98. https://doi.org/10.1016/j.jconrel.2009.02.013.

Lopes, L.B., Ferreira, D.A., De Paula, D., Garcia, M.T.J., Thomazini, J.A., Fantini, M.C.A., Bentley, M.V.L.B., 2006. Reverse hexagonal phase nanodispersion of monoolein and oleic acid for topical delivery of peptides: in vitro and in vivo skin penetration of cyclosporin A. Pharm. Res. 23, 1332–1342. https://doi.org/10.1007/s11095-006-0143-7.

Lopes, L.B., Speretta, F.F.F., Bentley, M.V.L.B., 2007. Enhancement of skin penetration of vitamin K using monoolein-based liquid crystalline systems. Eur. J. Pharm. Sci. 32, 209–215. https://doi.org/10.1016/j.ejps.2007.07.006.

Makvandi, P., Chen, M., Sartorius, R., Zarrabi, A., Ashrafizadeh, M., Dabbagh Moghaddam, F., Ma, J., Mattoli, V., Tay, F.R., 2021. Endocytosis of abiotic nanomaterials and nanobiovectors: Inhibition of membrane trafficking. Nano Today 40, 101279. https://doi.org/10.1016/j.nantod.2021.101279.

Mandal, A., Kumbhojkar, N., Reilly, C., Dharamdasani, V., Ukidve, A., Ingber, D.E., Mitragotri, S., 2020. Treatment of psoriasis with NFKBIZ siRNA using topical ionic liquid formulations. Sci. Adv. 6, 1–10. https://doi.org/10.1126/sciadv.abb6049.

Milak, S., Zimmer, A., 2015. Glycerol monooleate liquid crystalline phases used in drug delivery systems. Int. J. Pharm. 478, 569–587. https://doi.org/10.1016/j.ijpharm.2014.11.072.

Nemati, H., Ghahramani, M.H., Faridi-Majidi, R., Izadi, B., Bahrami, G., Madani, S.H., Tavoosidana, G., 2017. Using siRNA-based spherical nucleic acid nanoparticle conjugates for gene regulation in psoriasis. J. Control. Release 268, 259–268. https://doi.org/10.1016/j.jconrel.2017.10.034.

Nunes, K.M., Teixeira, C.C.C., Kaminski, R.C.K., Sarmento, V.H.V., Couto, R.O., Pulcinelli, S.H., Freitas, O., 2016. The Monoglyceride Content Affects the Self-Assembly Behavior, Rheological Properties, Syringeability, and Mucoadhesion of In Situ-Gelling Liquid Crystalline Phase. J. Pharm. Sci. 105, 2355–2364. https://doi.org/10.1016/j.xphs.2016.05.005.

Petrilli, R., Eloy, J.O., Praça, F.S.G., Del Ciampo, J.O., Fantini, M.A.C., Fonseca, M.J.V., Bentley, M.V.L.B., 2016. Liquid crystalline nanodispersions functionalized with cell-penetrating peptides for topical delivery of short-interfering RNAs: A proposal for silencing a pro-inflammatory cytokine in cutaneous diseases. J. Biomed. Nanotechnol. 12, 1063–1075. https://doi.org/10.1166/jbn.2016.2211.

Praça, F.S.G., Medina, W.S.G., Eloy, J.O., Petrilli, R., Campos, P.M., Ascenso, A., Bentley, M.V.L.B., 2018. Evaluation of critical parameters for in vitro skin permeation and penetration studies using animal skin models. Eur. J. Pharm. Sci. 111, 121–132. https://doi.org/10.1016/j.ejps.2017.09.034.

Ren, Q., Li, M., Deng, Y., Lu, A., Lu, J., 2021. Triptolide delivery: Nanotechnology-based carrier systems to enhance efficacy and limit toxicity. Pharmacol. Res. 165, 105377. https://doi.org/10.1016/j.phrs.2020.105377.

Rios, F.J., Touyz, R.M., Montezano, A.C., 2017. Isolation and Differentiation of Human Macrophages, in: Hypertension: Methods and Protocols, Methods in Molecular Biology. pp. 311–320. https://doi.org/10.1007/978-1-4939-6625-7_24.

Rodrigues, L., Schneider, F., Zhang, X., Larsson, E., Moodie, L.W.K., Dietz, H., Papadakis, C.M., Winter, G., Lundmark, R., Hubert, M., 2019. Cellular uptake of self-assembled phytantriol-based hexosomes is independent of major endocytic machineries. J. Colloid Interface Sci. 553, 820–833. https://doi.org/10.1016/j.jcis.2019.06.045.

Rosa, J., Suzuki, I., Kravicz, M., Caron, A., Pupo, A.V., Praca, F.G., Bentley, M.V.L.B., 2018. Current non-viral siRNA delivery systems as a promissing treatment of skin diseases. Curr. Pharm. Des. 24, 2644–2663. https://doi.org/10.2174/1381612824666180807120017.

Rossetti, F.C., Fantini, M.C.A., Carollo, A.R.H., Tedesco, A.C., Bentley, L.B., M.v.,, 2011. Analysis of Liquid Crystalline Nanoparticles by Small Angle X-Ray Diffraction: Evaluation of Drug and Pharmaceutical Additives Influence on the Internal Structure. J. Pharm. Sci. 100, 2849–2857. https://doi.org/10.1002/jps.22522.

Schön, M.P., 2019. Adaptive and Innate Immunity in Psoriasis and Other Inflammatory Disorders. Front. Immunol. 10, 5–9. https://doi.org/10.3389/fimmu.2019.01764.

Setten, R.L., Rossi, J.J., Han, S., 2019. The current state and future directions of RNAi-based therapeutics. Nat. Rev. Drug Discov. 18, 421–446. https://doi.org/10.1038/s41573-019-0017-4.

Shan, X., Gong, X., Li, J., Wen, J., Li, Y., Zhang, Z., 2022. Current approaches of nanomedicines in the market and various stage of clinical translation. Acta Pharm. Sin. B. 12 (7), 3028–3048. https://doi.org/10.1016/j.apsb.2022.02.025.

Siekmann, B., Bunjes, H., Koch, M.H.J., Westesen, K., 2002. Preparation and structural investigations of colloidal dispersions prepared from cubic monoglyceride–water phases. Int. J. Pharm. 244, 33–43. https://doi.org/10.1016/S0378-5173(02)00298-3.

Silvestrini, A.V.P., Caron, A.L., Viegas, J., Praça, F.G., Bentley, M.V.L.B., 2020. Advances in lyotropic liquid crystal systems for skin drug delivery. Expert Opin. Drug Deliv. 00, 1–25. https://doi.org/10.1080/17425247.2020.1819979.

Silvestrini, A.V.P., Debiasi, B.W., Praça, F.G., Bentley, M.V.L.B., 2022. Progress and challenges of lyotropic liquid crystalline nanoparticles for innovative therapies. Int. J. Pharm. 628, 122299. https://doi.org/10.1016/j.ijpharm.2022.122299.

Suzuki, I.L., de Araujo, M.M., Bagnato, V.S., Bentley, M.V.L.B., 2021. TNFα siRNA delivery by nanoparticles and photochemical internalization for psoriasis topical therapy. J. Control. Release. 338, 316–329. https://doi.org/10.1016/j.jconrel.2021.08.039.

Tan, A., Hong, L., Du, J.D., Boyd, B.J., 2019. Self-Assembled Nanostructured Lipid Systems: Is There a Link between Structure and Cytotoxicity? Adv. Sci. 6, 1801223. https://doi.org/10.1002/advs.201801223.

Thapa, R.K., Choi, J.Y., Poudel, B.K., Hiep, T.T., Pathak, S., Gupta, B., Choi, H., Yong, C. S., Kim, J.O., 2015. Multilayer-Coated Liquid Crystalline Nanoparticles for Effective Sorafenib Delivery to Hepatocellular Carcinoma. ACS Appl. Mater. Interfaces 7, 20360–20368. https://doi.org/10.1021/acsami.5b06203.

Tofani, L.B., Depieri, L.V., Campos, P.M., Riul, T.B., Antonietto, K.S., de Abreu Fantini, M.C., Bentley, M.V.L.B., 2018. In Vitro TyRP-1 Knockdown Based on siRNA Carried by Liquid Crystalline Nanodispersions: an Alternative Approach for Topical Treatment of Vitiligo. Pharm. Res. 35, 104. https://doi.org/10.1007/s11095-017-2330-0.

Tong, L.u., Zhao, Q., Datan, E., Lin, G.-Q., Minn, I.l., Pomper, M.G., Yu, B., Romo, D., He, Q.-L., Liu, J.O., 2021. Triptolide: reflections on two decades of research and prospects for the future. Nat. Prod. Rep. 38 (4), 843–860. https://doi.org/10.1039/D0NP00054J.

van 't Hag, L., Gras, S.L., Conn, C.E., Drummond, C.J., 2017. Lyotropic liquid crystal engineering moving beyond binary compositional space – ordered nanostructured amphiphile self-assembly materials by design. Chem. Soc. Rev. 46 (10), 2705–2731. https://doi.org/10.1039/C6CS00663A.

Viegas, J.S.R., Praça, F.G., Caron, A.L., Suzuki, I., Silvestrini, A.V.P., Medina, W.S.G., Del Ciampo, J.O., Kravicz, M., Bentley, M.V.L.B., 2020. Nanostructured lipid carrier co-delivering tacrolimus and TNF-α siRNA as an innovate approach to psoriasis. Drug Deliv. Transl. Res. 10 (3), 646–660. https://doi.org/10.1007/s13346-020-00723-6.

Wang, Y., Yang, C., Hu, R., Toh, H.T., Liu, X., Lin, G., Yin, F., Yoon, H.S., Yong, K.-T., 2015. Assembling Mn:ZnSe quantum dots-siRNA nanoplexes for gene silencing in tumor cells. Biomater. Sci. 3, 192–202. https://doi.org/10.1039/C4BM00306C.

Wang, B., Zhang, Y., Mao, Z., Gao, C., 2012. Cellular Uptake of Covalent Poly(allylamine hydrochloride) Microcapsules and Its Influences on Cell Functions. Macromol. Biosci. 12, 1534–1545. https://doi.org/10.1002/mabi.201200182.

Yan, Y.i., Liu, X.-Y., Lu, A.n., Wang, X.-Y., Jiang, L.-X., Wang, J.-C., 2022. Non-viral vectors for RNA delivery. J. Control. Release 342, 241–279. https://doi.org/10.1016/j.jconrel.2022.01.008.

Yang, M., Gu, Y., Yang, D., Tang, X., Liu, J., 2017. Development of triptolide-nanoemulsion gels for percutaneous administration: Physicochemical, transport, pharmacokinetic and pharmacodynamic characteristics. J. Nanobiotechnology 15, 1–15. https://doi.org/10.1186/s12951-017-0323-0.

Yuan, K., Li, X., Lu, Q., Zhu, Q., Jiang, H., Wang, T., Huang, G., Xu, A., 2019. Application and Mechanisms of Triptolide in the Treatment of Inflammatory Diseases—A Review. Front. Pharmacol. 10, 1–12. https://doi.org/10.3389/fphar.2019.01469.

Zhang, L., Chang, J., Zhao, Y., Xu, H., Wang, T., Li, Q., Xing, L., Huang, J., Wang, Y., Liang, Q., 2018. Fabrication of a triptolide-loaded and poly-γ-Glutamic acid-based amphiphilic nanoparticle for the treatment of rheumatoid arthritis. Int. J. Nanomedicine 13, 2051–2064. https://doi.org/10.2147/IJN.S151233.

Zhang, Y., Fry, C.G., Pedersen, J.A., Hamers, R.J., 2017. Dynamics and Morphology of Nanoparticle-Linked Polymers Elucidated by Nuclear Magnetic Resonance. Anal. Chem. 89, 12399–12407. https://doi.org/10.1021/acs.analchem.7b03489.

Zhao, E., Zhao, Z., Wang, J., Yang, C., Chen, C., Gao, L., Feng, Q., Hou, W., Gao, M., Zhang, Q., 2012. Surface engineering of gold nanoparticles for in vitro siRNA delivery. Nanoscale 4, 5102–5109. https://doi.org/10.1039/c2nr31290e.